Design of demountable iSRR connectors on oversized holes subjected to wheel loading

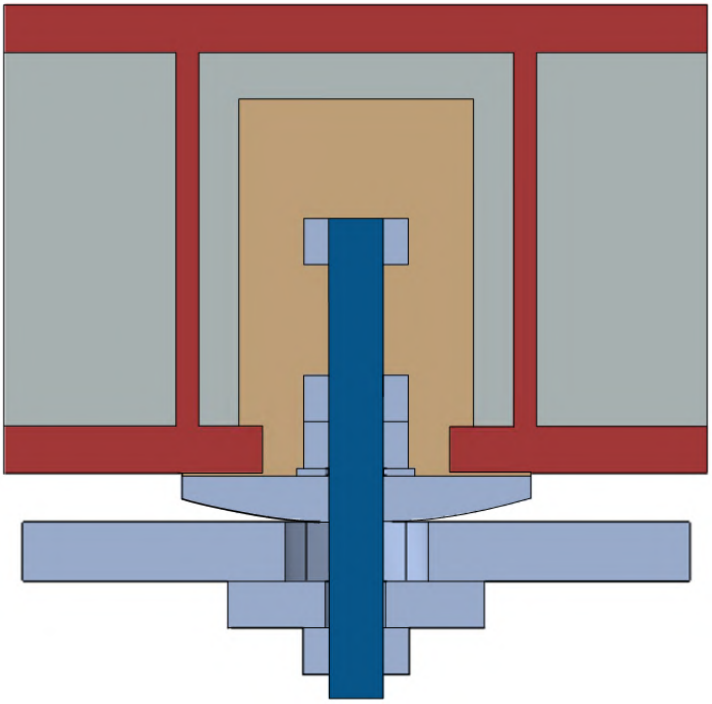

Jelco Köhlenberg

Design of demountable iSRR connectors on oversized holes subjected to wheel loading

Jelco Köhlenberg

to obtain the degree of Master of Science
in Structural Engineering
at the Delft University of Technology

to be defended publicly on
Wednesday 29 September 2023 at 11:00

Student number:	4677382	
Thesis committee:	Dr. Marko Pavlović	*Committee Chairman*
	MSc. Angeliki Christoforidou	*Daily Supervisor*
	ir. Sander Pasterkamp	*External Committee Member*

Preface

The thesis you have in front of you is the result of 7 months of work on one of the younger fields in the construction industry: bolted connections in FRP applications. After seeing the results and the potential of the project, I can say that I fully believe in its future. I hope that many will find interest in this project, and that some may continue with it.

First of all, I would like to thank Marko Pavlović for his very supportive way of giving feedback and his enthusiasm and belief in the project. I would like to thank Sander Pasterkamp as the external committee member, as his insights in the practical application of the project increased the usability of the connector. As the last member of the thesis committee I would like to thank Angeliki Christoforidou, for her constant support and the ability to come by her office whenever needed.

Furthermore I would like to thank Abishek Baskar, a fellow MSc. student working on a closely related topic. His constant enthusiasm and support in the lab helped me tremendously. In his words, our theses combined felt like a group project. In addition I would like to thank Giorgos Stamoulis, lab technician at the TU Delft, for his support in the lab even if the time on hands was short.

At last it is important to acknowledge the help outside of the direct engineering of the project. Without the support from my parents or my girlfriend I would have been a lot more stressed than necessary, and enjoyed the process a lot less than I eventually did. Thank you for your constant belief in me, you give the small nudges that make it all a lot more fun.

Jelco Köhlenberg
Delft, September 2023

Summary

As many bridges in the Netherlands are past their design-life and yet still have well-functioning steel superstructures, their bridge decks are often due to be replaced. FRP panels are promising alternatives to concrete decks for these renovation works due to their low density, fast on-site construction time, and excellent acoustic and thermal properties. Many of these bridges are originally designed with hybrid interactions occurring at the connection level. Multiple connection types exist to ensure hybrid interaction with FRP decks. However, there is a gap in this field concerning a rapidly demountable connection able to transfer shear forces at girders with oversized holes. The injected reinforced resin connector is designed and aimed at achieving hybrid interaction through combined injection and preloading of the connector. The aim of this thesis is to find a viable design for this connection, and to test the connection under local compressive wheel loads. be able to design the connector and test it according to standards as expected to occur in real bridge applications, a FE-model of the bridge Nieuw-Vossemeer is made to assess expected loadlevels in the connection. The result is a combined list of loadlevels and geometrical tolerances that the connection will have to be able to sustain or perform under. Based on the resulting design requirements a main design is proposed. Here a steel bolt is embedded in the bridge deck and held in place by injection with reinforced resin. A steel plate separates the bridge deck from the girder flange, and creates a full steel clamping package. Multiple design alternatives are tested by the use of FE-models, where the variable is the type of steel plate used between the bridge deck and the girder flange. The most viable design to continue experimental tests with is selected by its stiffness, ultimate resistance, and a qualitative assessment regarding expected cyclic endurance. The best performing concept is a steel plate with a spherical bottom, a diameter of 150mm and maximum thickness of 20mm. Extra FE-analyses are performed on a local scale, and take into account positional deviations from the most ideal situation. In addition a series of two static and two cyclic experiments has been performed. Apart from finding their respective resistances, the failure modes are assessed and compared together with the numerical analysis.

The static tests show an ultimate resistance of 501kN, the numerical analysis shows a resistance of 498kN. Both the static tests and the numerical analysis failed ultimately due to delamination in the bottom facing of the FRP, the cyclic tests failed under a similar failure mode in the bottom FRP flange. On loading ranges with R = 0.1 it is found that the primary failure mode is a horizontal crack opening up in the bottom FRP flange, which propagates into the webs. The connection withstood 2 million cycles at 9kN - 90kN without damage. Subsequently, two different loadranges were applied to the two different tests, which failed after 394 thousand cycles at 13.5kN - 135kN and 34 thousand cycles at 18kN - 180kN. It is concluded that the spherical plate is able to function as a coverplate and withstands rotations, displacements and the required loadlevels as expected in bridge applications. The primary recommendation is to continue performing tests with a similar plate with a thickness of 15mm, as the current design overshoots the required resistance significantly.

The results show that the design is well able to sustain the required local compressive wheel loads, both in ultimate and cyclic resistance. With the ability to (de)mount these FRP panels quickly on-site, two main goals have been reached. Firstly, this brings the use of FRP panels in infrastructure closer, leading to reduced loads onto steel superstructures of existing bridges (and hence an extended lifetime). Secondly, a fundamental step has been set towards modular bridge design, where during failure only specific panels of the system have to be replaced. Together these developments can lead to a reduced impact of the construction industry on the environment.

Contents

Preface i

Summary ii

1 Introduction 1
1.1 Research Question . . . 2
1.2 Methodology . . . 2

2 Literature Review 4
2.1 FRP Bridge Decks . . . 4
2.1.1 Pultruded Panels . . . 4
2.1.2 Vacuum Infused Panels . . . 5
2.2 Hybrid Interaction . . . 6
2.2.1 Welded Headed Studs . . . 7
2.2.2 Blind Bolting . . . 7
2.3 FRP Joining Methods . . . 8
2.3.1 Adhesive Bonding . . . 8
2.3.2 Mechanical Fastening . . . 8
2.3.3 Injected Mechanical Connections . . . 9
2.4 iSRR Connector . . . 10
2.4.1 Shear Resistance . . . 11
2.4.2 Wheel Loading . . . 12
2.5 Conclusions . . . 13

3 Requirements 15
3.1 Numerical Model . . . 15
3.2 Loads - Ultimate Limit State . . . 16
3.2.1 LM2 . . . 16
3.2.2 LM1 . . . 17
3.3 Loads - Fatigue Limit State . . . 17
3.3.1 FLM3 . . . 18
3.3.2 FLM4 . . . 18
3.4 Geometrical Requirements . . . 19
3.4.1 Steel Girders - Oversized Holes . . . 19
3.4.2 Deck Clearance: Out-of-Straightness of the FRP Deck . . . 20
3.4.3 Angular Deviation . . . 21
3.5 Conclusions . . . 21

4 Numerical Analysis 22
4.1 Design Concept . . . 22
4.2 Model Description . . . 23
4.2.1 Material Models . . . 24
4.2.2 Loading and Boundary Conditions . . . 24
4.2.3 Interactions . . . 24
4.2.4 Mesh . . . 25
4.3 Resistance and Behaviour of the Alternatives . . . 26
4.3.1 SP15 . . . 26
4.3.2 SP20 . . . 27
4.3.3 CU20 . . . 27
4.3.4 PP20 . . . 28
4.3.5 Choice of alternative . . . 28

4.3.6 Conclusion . . . 29

5 Numerical Analysis of SP20 **30**
5.1 SP20 - Standard Situation . . . 30
5.1.1 Failure Mechanism . . . 31
5.1.2 Preload Force . . . 32
5.2 Angular Deviation . . . 33
5.3 Off-Centered Placement . . . 35
5.4 Conclusions . . . 36

6 Experimental Campaign **37**
6.1 Production of the Specimens . . . 37
6.2 Static Tests . . . 38
6.2.1 Test Set-Up . . . 38
6.2.2 Results and Failure Modes . . . 39
6.2.3 Preload Loss . . . 40
6.2.4 Comparison Numerical and Experimental Results . . . 41
6.3 Cyclic Tests . . . 43
6.3.1 Test Set-Up . . . 43
6.3.2 Results . . . 44
6.3.3 Failure Modes . . . 46
6.3.4 Preload Loss . . . 47
6.3.5 F-N Curve . . . 48
6.4 Conclusions . . . 49

7 Recommendations **50**

8 Conclusions **51**

References **52**

A Material Properties Numerical Model **55**

B Design Dimensions **57**

C Failure Progression **58**

D Cyclic Test Goals **59**

1 Introduction

The Netherlands is well known for its large amount of water and the bridges that come along with it. The majority of these bridges have been built between the 1960s and the 1980s, meaning that about one third of these bridges are past their design life and not yet renovated (Ruben Messelink and Simone Tukker, 2018). On top of that, the intensity of traffic changed drastically over the years, and heavier types of transport became standard. The bridges now have to endure heavier and more frequent loads, leading to shorter structural lives than originally designed for. Rapid action is needed to mitigate the heavy damage and resulting restrictions on allowed traffic types.

Not all of the affected bridges need work on the main bearing system and, for many, it is sufficient to modify only parts. A common failure mode, or mode of deterioration, is the cracking of concrete bridge decks and consequently the corrosion of the steel reinforcement in these panels. In these cases, it is arguably economically and environmentally beneficial to change only the bridge decks instead of the entire bridge, given that the main girders are still fully functional.

The industry standard for bridges used to be concrete decks or steel orthotropic panels. It is possible to produce concrete decks with bolted connections, allowing for demounting and the general capability of delivering full hybrid interaction between the concrete deck and steel girders. Due to concrete cracking and the roadways being worked with salts in the winter, these decks are prone to suffer from corrosion.

Recent studies indicate that FRP could be a viable alternative material to concrete in the bridge decking application. The most important advantages are listed as (Sotelino et al., 2001):

1. FRP is a lightweight material, with a self-weight of approximately $1200kg/m^3$, versus $2600kg/m^3$ for concrete and $7850kg/m^3$ for steel.
2. FRP is corrosion resistant, which does not hold for the steel reinforcement in concrete decks.
3. FRP is chemically more resistant than concrete.
4. FRP has a higher strength than steel and concrete.
5. Specifically for GFRP, the fatigue performance is characterized by higher allowable stresses than steel for the same amount of cycles. FRP's also have a flatter S-N curve. However, no fatigue life limit exists for FRP.

In recent years, multiple bridges fully made of FRP have been constructed. These are generally bicycle and pedestrian bridges (Ali et al., 2021). They are interesting as a concept, but generally very expensive due to their specific formwork. Economically, these bridges could become interesting if many of them are produced, such that the cost of formwork per bridge would reduce. A good starting step towards that is making FRP the bridge deck standard in the industry. With generally standard shapes and sizes, the formwork can be reused time and time again.

The main limitation in bridge retrofitting with FRP decks is the composite interaction that has to be achieved between the main girders and the decks. It is currently possible, but only if the bridge decks are adhesively bonded to the steel girders. By making use of adhesive bonding, it becomes hard (or almost impossible) to demount these bridge decks when needed. As such, the need arises for a bolted connection between the FRP decks and the steel girders. Research is going on at the TU Delft towards

the injected Steel Reinforced Resin (iSRR) connector, which should bridge this gap in the industry and create a connector able to sustain shear loads as well as large wheel loads.

1.1. Research Question

The research presented in this report is aimed at the improvement of the design of the iSSR connector, such that it can sustain sufficient local wheel loading levels when mounted on oversized holes. As such, the main research question of this thesis is as follows:

What does a well-designed iSRR connector look like, when designed for the expected local wheel load levels and geometrical deviations occurring in bridge-applications?

Multiple research questions will be answered first to end up with an efficient design:

1. What are the requirements of the iSRR connector, both in load-levels to sustain, as well as the positional tolerances and geometrical deviations?
2. What design concepts improve the wheel loading resistance of the connector, while allowing for hybrid interaction?
3. What are the resistances and failure modes of the connector under cyclic and static loading?

1.2. Methodology

First, a literature study will be performed to gain more insights in the current state-of-the-art regarding FRP decks and connection methods. This literature study will review the background and findings in topics closely related to the subject, for example the different types of bridge decks available and their typical failure modes. Bolted connections allowing hybrid interaction in bridges with other materials (steel / concrete) will be examined, as well as the currently used types of joining techniques in steel girder to FRP bridge decks connections. This literature study can be found in Chapter 2.

Chapter 3 covers the first research question. This chapter is split into two main sections: loadlevels, and the design requirements and tolerances to take into account.

Chapter 4 and 5 are aimed at the design of different alternatives, producing a FE-model and verifying the connection based on the requirements found in Chapter 3. First, multiple FE-models are produced to assess different alternatives. After a design is deemed the most favourable, the models will be refined and used for gaining a deeper understanding of the failure modes of the connection.

Chapter 6 at last covers the experimental campaign where static and cyclic tests are performed. The results of these tests are compared with the results from the FE-models. Figure 1.1 shows a flowchart explaining the methodology in a short overview.

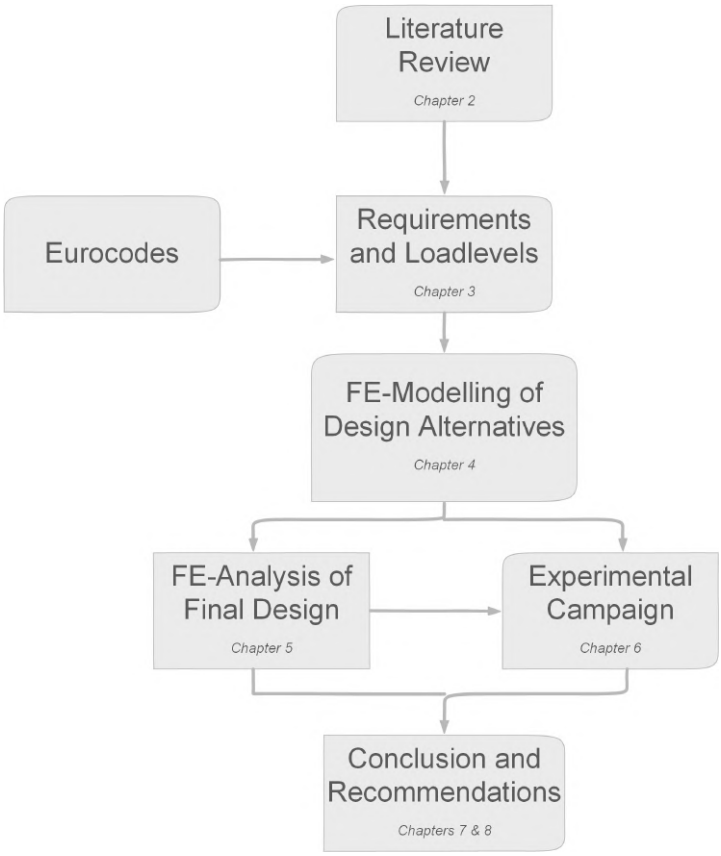

Figure 1.1: Flowchart of the research order

2

Literature Review

FRP (Fibre Reinforced Polymer) is a composite material, meaning that it is a combination of fibres and a polymer matrix. With a high strength to density ratio, the material is very suited to be used as a bridge deck due to the low dead loads imposed by the light material. Furthermore, FRP decks are rapid in erection, and have relatively low carbon emissions (Mara et al., 2014). The low carbon emissions not only relate directly to the production of the material, but also to the low demands for transport, given that the material is very lightweight. These reasons contributed to the rapid rise of the use of FRP and composites in general in the 1980s (Ali et al., 2021). As mentioned, FRP is also very competent for usage in the construction industry. This can be either by producing full bridges, or just parts of bridges, out of FRP. This practice started to gain popularity around the 1990s-2000s with complete FRP bridges in (Qureshi, 2023), especially when the first FRP roadbridge was constructed in the UK in 1995.

2.1. FRP Bridge Decks

FRP decks can be produced in a few different ways, of which pultrusion and vacuum infusion are the most often used ones. Pultrusion is an advantageous production method for mass-production of structural elements, but the choice of fibre-direction is limited to the primary longitudinal direction. Vacuum infusion allows for a more tailored design, resulting in an allowable deck span of about 10m vs 3m with pultrusion (Bakis et al., 2002). This section will briefly discuss both production methods. Furthermore this section will describe in more detail sandwich panels / vacuum infused panels, its benefits and typical failure modes.

2.1.1. Pultruded Panels

Pultrusion is a production method specifically suitable for structural elements with constant cross-sections, as well as elements which are of great length (Joshi, n.d.). The normal type of pultrusion is that of where a material is pushed through a mold, creating the cross-section, and by continuing to do so an entire element is created. FRP cannot be pushed through a mold since the fibres do not have any bending stiffness, such that the production process looks a bit more like Figure 2.1.

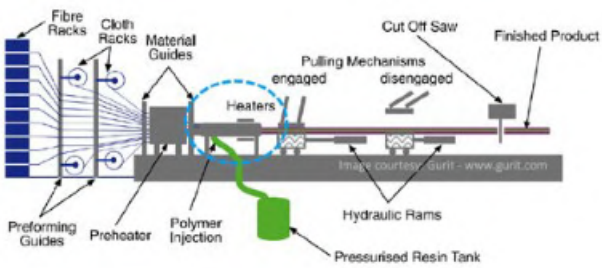

Figure 2.1: Pultrusion production process (Composites World, 2020)

Due to the nature of the production process, fibres are only able to lie in the longitudinal (0 degrees) direction. Since a bridge panel spans perpendicularly to the driving direction, the fibres lie in that direction as well, spanning from girder to girder. These fibres do not provide shear strength in plane, such that only the matrix takes up shear and hence a limited span can be reached.

Typical cross-sections are depicted in Figure 2.2. Each deck works as a beam in normal fibre direction, but in the transverse direction this action cannot be provided due to discontinuity in fibres. The cross-sections depict different ways of dealing with this problem. Number (a), (c), and (e) work largely with truss interactions, where (d) uses Vierendeel interaction. The stiffness and strength in this transverse direction is a lot lower, and matrix cracking is quickly expected here. In a study on the 4-point bending behaviour of these types of decks, it was found that the main failure modes were debonding and punching at the point of loading (Alagusundaramoorthy et al., 2006). Especially the latter is disadvantageous for the application in a hybrid bridge system, where its members are jointed by a bolted connection.

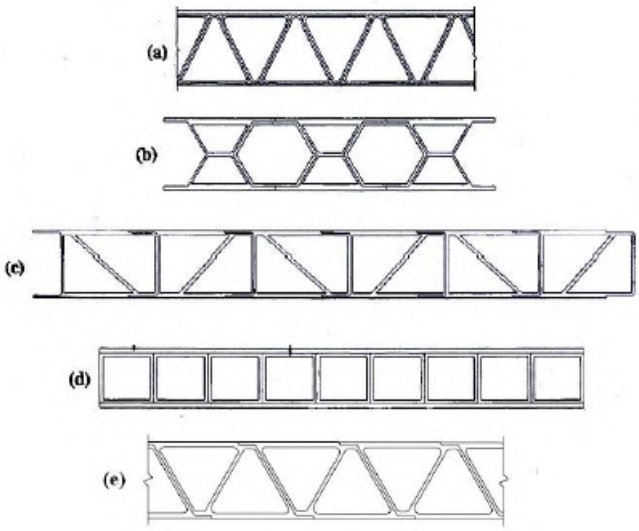

Figure 2.2: Pultrusion sections: (a) EZ-span system; (b) Superdeck system; (c) DuraSpan system; (d) Strongwell system; (e) ASSET system (Mara, 2011)

2.1.2. Vacuum Infused Panels

The process of vacuum infusion (Vacuum-Assisted Resin Transfer Molding (VARTM)), is not as automatic as the above mentioned pultrusion process. With VARTM, a mold is made in which foam cores or other filler materials are placed. Around these cores the fibres (or fibre mats) are wrapped, after which the mould is hermetically closed off. By injecting resin from one side and creating a vacuum, the resin will travel through the mold and create a unified piece of material, the FRP deck. The following differences between the two processes can be noted:

1. VARTM is less automatized. Large scale production is easier with pultrusion.
2. VARTM creates a more adjustable cross-section, specific to the needs, where pultrusion can only produce a constant cross-section.
3. Where pultrusion can only produce fibres in the 0° direction, VARTM can have fibres in all direction, drastically improving shear loading behaviour.

This production process leads to two FRP flanges on the top and the bottom of the panel with a core of filler material in between. This core has generally a lower density than the FRP itself, and by increasing its height a major increase in stiffness to weight ratio for the same thickness of FRP flanges can be reached (see Figure 2.3).

Typical failure modes of a deck produced by the method of VARTM are given as: fibre failure, matrix failure, fibre-matrix debonding, and interface delamination (R. Koloor et al., 2018). Specifically for ultimate load tests, it was found that sandwich panels can fail suddenly due to the effects of delamination

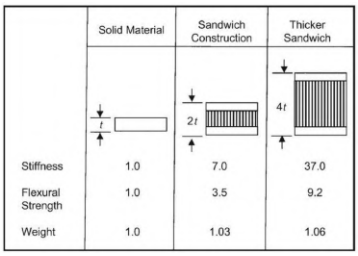

Figure 2.3: Increasing stiffness/weight ratio in sandwich panels (Campbell, 2010)

and debonding (Kulpa and Siwowski, 2019). During cyclic loading, apart from failure modes, stiffness reduction is of importance. Specifically for sandwich panels with integrated webs it is found that panels can expect up to 6.5% increase in global deflections for a 60kN wheel load (Koetsier, 2021).

Debonding of the face and the (foam) core is one of the most important failure modes in sandwich panels. The failure is started and continued as:

1. Impact loads lead to a small debonding of the top face and the core.
2. Rolling loads increase the gap created in step 1.
3. Once the gap is large enough, the top face cannot bear the shear forces anymore, and full delamination takes place

The InfraCore technology accounts for this by applying fibres from the top face continuously to the bottom face in all directions, such that there are no resin-dominated areas. By stacking many of these continuously produced Z-shapes as in Figure 2.4, the InfraCore technology is created to be non-debonding.

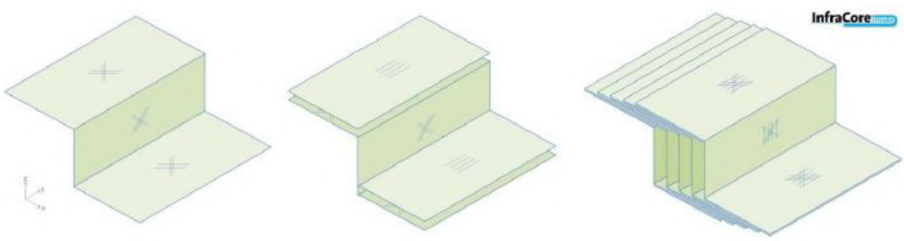

Figure 2.4: Stacking Z-shapes (InfraCore, 2023)

In the 4-point bending test of sandwich panels it was specifically found that no punching shear occurred at any point (Alagusundaramoorthy et al., 2006), but that foamcore debonding and web-buckling were the dominant failure modes. By applying the InfraCore technology, only the web-buckling remains of significance, which is easy to overcome by merely thickening the webs.

2.2. Hybrid Interaction

Hybrid interaction in bridge systems is a characteristic that is important to define properly. Due to hybrid interaction, systems work together (in this case the steel girder and FRP deck), and these systems transfer loads to each other. It can be very desirable to design for hybrid interaction, since effectively the two elements get combined into one cross-section, working fully together. Bending moments get distributed over the full cross-section, rather than that the two cross-section each take up a portion of the bending loads. Important is that these elements cooperate fully, and hence have the same deflection. A classical hypothesis is that at the interface between the two elements no slip can occur (Correia et al., 2007).

The amount of hybrid interaction that is desired can be achieved by proper design decisions: if it is desired to not have hybrid interaction, it should be made sure that there is no shear force transfer possible between the deck and the steel girder. This directly explains the crux of the problem, that if hybrid interaction is desired, that shear force should be fully transferable at the joints. This section will briefly cover types of joints that allow for hybrid interaction, without being limited to just FRP-steel joints.

2.2.1. Welded Headed Studs

Welded headed studs are shear connectors that are specifically used in concrete decking applications. The studs are welded on the steel beam or sheet, the concrete is poured on the form work, and when the concrete hardens, the studs are embedded in the concrete. These studs are not at all demountable since they are welded to the steel beam and embedded in the concrete. The only way of separation is therefore by breaking the concrete. Figure 2.5 shows the layout of such a connection, of which the typical failure modes under shear are as follows (Lam, 2007):

1. Concrete crushing in compression.
2. Yielding of the headed stud.
3. A combination of the above.

Even though this connection type works well, it is in no way demountable, which is an important aspect of the scope for this project.

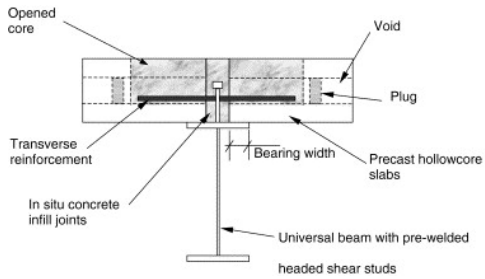

Figure 2.5: Welded headed studs (Lam, 2007)

2.2.2. Blind Bolting

Blind bolting is the practice of using bolts that only need to be tightened from one side, where the other side of the bolt is tightly embedded in a material. An important advantage of this type of connection is that it is demountable, and hence very applicable for retrofitting. For concrete this technique is not yet often used, since it is found that welded studs are superior to the bolted alternatives. A study by Jung et al. (2022a) shows that for a standard push-out test it holds that a standard blind bolt experienced initial fracture at a load of 48% of that of its welded counterpart, and also that the welded stud shear connector is superior in its ductile behaviour. This finding is however opposed to by Pathirana et al. (2016). In this study, conventional welded headed studs were compared with blind bolted rivets in a standard push-out test. Important findings here are that blind bolted rivets experience a much higher ultimate strength, but that they have much lower stiffness as well. However, most of the slip in blind bolted rivets happened before yielding, where 90% of slip happened in welded studs after yielding of the connector.

Multiple types of blind bolts are given in Figure 2.6. These bolts range from relatively standard blind bolts (b,c and d) where bolts are embedded with or without a nut, to friction grip bolts and special design solutions. Findings give that the embedded bolts without a nut give low ultimate shear strength, at about 80% of normal welded studs. Double embedded nuts give a higher shear strength and general performance than single embedded nuts (Zhang et al., 2019), but how much the increase in strength and stiffness actually is, is not given. However, different studies describe that the ultimate strength of single embedded nuts and double embedded nuts are found to be similar (Pavlović, 2013). The actual resistance of these connectors appears to be very situation specific, and depends a lot on the geometry as well.

Figure 2.6 shows more possible connectors, from which number (a) to (e) are embedded in grout, and therefore the bolt itself cannot be replaced, which would be favourable if the bolt yielded or when the concrete/grout crushed under compression forces. Bolts (f) and (g) do give this option, but only for yielding of the lower part of the bolt, and not for concrete crushing or any yielding in the embedded steel coupler.

Connection (f) specifically consists of two bolts, a short and long one, and a coupler between the two bolts. The lower bolt can be replaced and post-installed, where the upper bolt cannot be replaced once

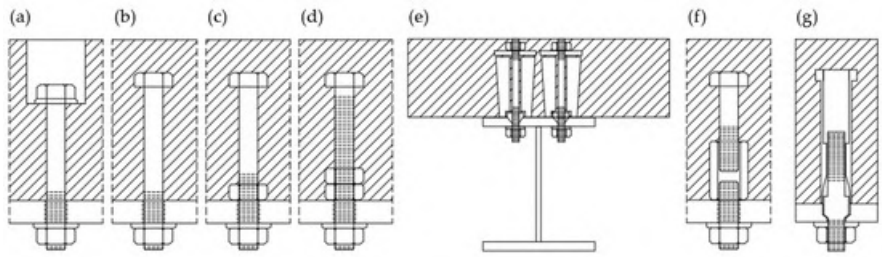

Figure 2.6: Multiple demountable shear connectors: (a) friction grip bolt; (b) without embedded nut; (c) with embedded nut; (d) double embedded nuts; (e) LNSC; (f) novel bolted connectors; (g) LBDSC (Jung et al., 2022b)

it is embedded. The connection gives similar results to a conventional welded stud in a static push-out test as to evaluate the ultimate strength, but also for this connection it holds that the slip deformation is higher for the bolted connection than for the welded studs (Yang et al., 2018).

The friction grip bolt is part of a connection where by preloading the bolt friction is generated between the concrete slab and the steel girder. Pavlović (2013) described that friction can lead up to an increase of 30% of shear resistance compared to standard welded studs connectors (M12), but that these effects decrease with increased bolt diameter, to for example only a 10% increase in shear resistance for an M24 bolt.

2.3. FRP Joining Methods

A barrier in the current state of industry towards adaptation of FRP bridge panels is the lack of a predictable connector regarding fatigue loading. Multiple FRP joining methods are available on the market and used in modern construction engineering, each with their own limitation. Generally, the options can be divided in the following categories:

1. Mechanical fastening
2. Adhesive bonding
3. Hybrid joints

This section will briefly discuss the options currently on the market, their (dis)advantages, and research to new types of connectors, including FRP-Steel connectors.

2.3.1. Adhesive Bonding

Adhesive bonding is a cost-effective and easy method to connect FRP bridge decks to the main steel girders. The process is like gluing something, applying an epoxy between the two elements creates a continuous bond between the two elements. The method can create fully hybrid bonds, which means that the bridge deck can be used as a top chord in compression of the girder-system, and that the adhesive layer can transfer all shear forces as needed (Keller and Gürtler, 2005a).

A specific research executed by Güller (2005), shows that it is very viable to use adhesively bonded FRP-decks as hybrid systems. In this research positive bending of the system was examined, such that the FRP-deck is fully in compression. The failure mechanism of this system eventually lied in compressive failure of the FRP-deck, while the steel girders were already yielding. An additional behaviour of adhesive bonds is that there is no fatigue life occurring, as well as no creep behaviour (Keller and Gürtler, 2005b).

2.3.2. Mechanical Fastening

Mechanical fastening constitutes all possible types of connections where the transfer of forces is not created by adhesive (continuous) bonding. The most common and known type is standard bolting, which has similar failure properties to rivets. Rivets are easy to install, but provide less precision compared to bolts, as well as a lower fatigue strength (Troughton, 2008). Therefore, only bolts will be further assessed in this review.

Bolts used in FRP design are usually made of steel due to their high stiffness and strength, where bolts out of FRP have too little stiffness to create hybrid interaction. Bolts are well demountable and

easy to install, but have the drawback of posing high concentrated loads at and around the bolt holes. For bolts, the most typical types of failure under shear are given as (Abdelkerim et al., 2019):

1. Bearing failure
2. Shear-out failure
3. Net tension failure
4. Cleavage failure
5. Bolt Failure
6. Punching failure (as in concrete)

Brittle failure modes are to be avoided, where ductile failure modes are preferred. The latter type occurs slowly, and is seen with bearing failure, which makes bearing failure the preferred dominating type of failure in bolted connections (Mottram and Turvey, 2003).

It is furthermore seen that hybrid interaction is much harder to achieve with mechanical fasteners than with adhesive bonding. The literature used to state that this is generally not possible, specifically for joining FRP with steel by using blind bolts (Zhou and Keller, 2005). In the more recent literature it is stated to be possible, but that the stiffness of the connection in shear is the main limitation to the bending stiffness of the composite (Satasivam et al., 2017). Satasivam et al. (2017) conducted experiments with blind bolts in FRP-steel single lap joints, with the joint as displayed in Figure 2.7. he blind bolts succeeded in almost full hybrid interaction, but still the slip was too high to be able to claim full hybrid interaction.

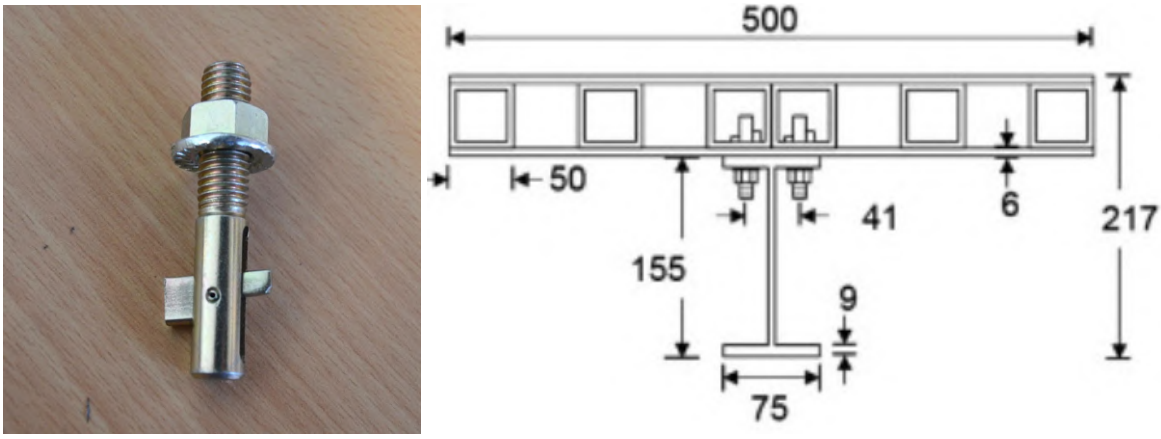

(a) Blind bolt **(b)** Blind bolt used in girder-deck construction

Figure 2.7: Blind bolts in FRP deck - steel girder construction (Satasivam et al., 2017)

Figure 2.8 shows a connection based on steel sleeves. The bolt, or headed stud, creates a clamp between the top steel sleeve and the beam flange, reducing the possible amount of uplift of the FRP deck. Furthermore the sleeve sleeves allow for redistribution of bearing forces in the FRP, which creates a higher resistance of the total connection. However, the slip found in the connection is relatively large, such that only 25% of full composite interaction can be achieved. The connection does excel in its fatigue endurance, as it can withstand an equivalent 75 years of loading cycles, which corresponds to 10.5 million loading cycles at a loading range of 11kN to 35kN.

2.3.3. Injected Mechanical Connections

Hybrid interaction relies heavily on the stiffness of a connection, and it is seen that mechanical fasteners allow for too much slip to have a high stiffness. This slip can be prevented by the use of injected bolted connections and by preloading of the connection and thus creating friction forces. The latter is with regards to composites not a very attractive method, as the through thickness creep of composites is relatively high and thus loses preload force easier. This section will discuss a few of the available and researched types of connections.

The first concept is a direct adaptation of the shear studs as used in conventional steel - concrete welded studs with injected grout. In an older study, the shear behaviour of three different types of

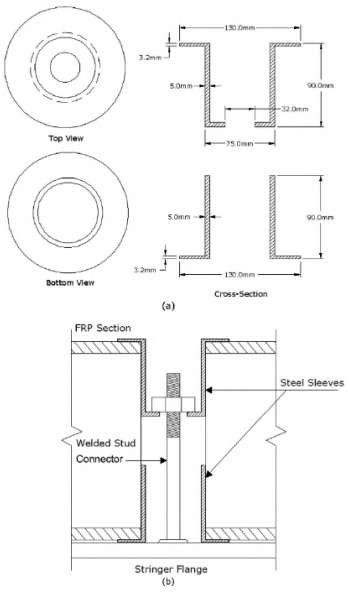

Figure 2.8: Steel sleeve connection (Davalos et al., 2011)

connections with studs welded to a steel beam and confined with grout in the FRP has been examined, see Figure 2.9.

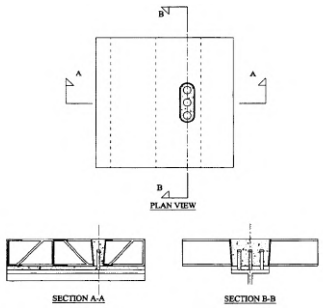

Figure 2.9: Welded studs, confined in the FRP with grout (Moon Ii et al., 2002)

The common types of failures modes observed were that of 1. loss of grout confinement, followed by 2. bearing of the stud in the bottom facing. Solutions that can contribute were given to be 1. a larger grout volume to redistribute the stresses more, and 2. a thicker bottom facing of the FRP to cope with the bearing stresses. The experimental capacity was found to be 104kN in a conventional push-out shear test.

A different study compared the use of injected bolts versus that of normal bolts in FRP shear push-out tests. Injected bolts reportedly have numerous practical advantages over standard bolts to for example the finishing edges of the FRP deck. Moreover from a design point of view, the injected bolts offer: 1. a higher stiffness, 2. the possibility to use larger clearance holes, and 3. a better fatigue performance (van Wingerde et al., 2002).

Figure 2.10 shows the fatigue performance of the injected bolts versus the normal bolts in a push-out test. The results show comparable performance for the ultimate load and the fatigue test with R = 0.1. However, once the cyclic load switches directions, as is the case for the tests with R = -1, the fatigue life of the injected bolts is expected to be about 3 times longer than that of the standard bolts at the same force range.

2.4. iSRR Connector

The iSRR (injected Steel Reinforced Resin) connector is a project under development at the TU Delft. The connector aims at closing the gap in the industry for full adaptation of hybrid steel - FRP bridges, by

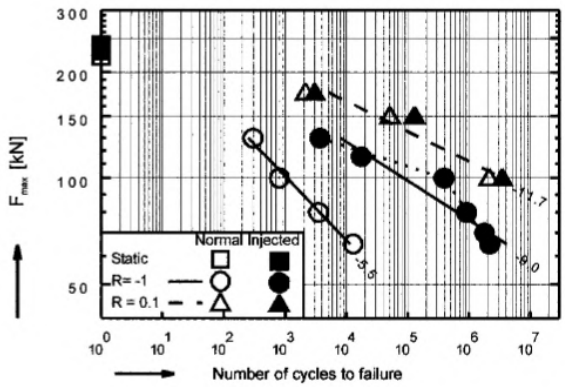

Figure 2.10: Fatigue performance of injected bolts vs. normal bolts (van Wingerde et al., 2002)

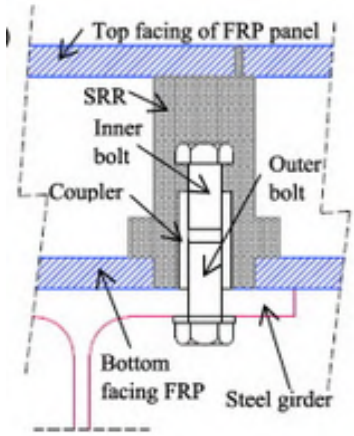

Figure 2.11: Initial design of the iSSR connector (Csillag and Pavlović, 2021)

creating a demountable connector that allows for full composite behaviour between the steel girders and the FRP bridge deck. As shown in the previous section, the injection of bolts closes the drilled holes and therefore creates a connection with very little initial slip, and hence a higher eventual stiffness. However, these injected bolts need to be accessed from both sides to be installed, which is not preferable as to leave the bridge deck as mostly intact as possible, as well as that it is generally more convenient to work only from one side of the bridge deck. The iSRR connector aims at the use of the combination between injected bolts and blind bolts, by preparing the bolts into the deck, which already could be done in an assembly hall, as to place these decks on location on the girders, where only the nut from the bottom of the girder has to be tightened. Afterwards this bolt is preloaded by tightening, preventing slipping in the steel plate. The iSRR connector hence combines two important methods of preventing slip. First the bolt is secured in the bridge deck by injection, and is afterwards preloaded to minimize slip at the level of the steel girder. Various designs have been examined, the first was that as in Figure 2.11.

The connector makes use of Steel Reinforced Resin. The basic concept is that a gap or hole is filled with steel shot balls, after which the leftover voids are filled up with resin. The use of the resin remains necessary, as otherwise rigid body movement is easily reached. Due to the use of the steel shot and the resin the stiffness of iSSR is 1.5-2 times higher than a standard resin injected connection (Nijgh, 2017).

2.4.1. Shear Resistance

The initial tests of the iSRR connector were conducted in a thesis comparing the push-out behaviour of the iSRR connector to two standard types of blind bolts available (Csillag and Pavlović, 2021). 9 push-out tests were performed, where it is important to note that the set-up differed from the standards.

A standard push-out test uses 8 shear bolts, but this led to delamination in the FRP deck, with very little damage around the shear connectors. The solution applied in this case was to use just 4 shear connectors, leading to better damage results around the shear connectors.

The ultimate load for the iSRR connector was somewhat lower than that of the conventional blind bolts, with respectively 120kN and 207.4kN / 164.3kN. This result is in contrast with a later study performed with partially the same research group, where in a single-lap joint the resistance of a single shear connector was found to be 160kN (Olivier et al., 2021). The load slip behaviour of the conventional steel blind bolts was mostly governed by ovalising of the FRP-plate, followed by deformation of the bolt. A found result is that the use of a nut or head at the end of the bolt in the deck leads to catenary effects in the bolt, preventing rotation of the bolt. The iSRR connector suffered from brittle bolt failure, and hence needed more ductility. The solution of a larger ratio of resin over bolt size is offered. Figure 2.12 shows the different load slip curves per component. It can be seen that initially compression of the FRP panel is dominant, but gets overtaken later by the deformation of the bolt and the crushing of the SRR.

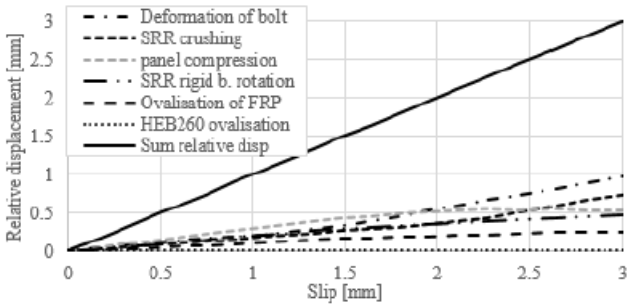

Figure 2.12: Load slip diagram of the iSRR connector for each component (Csillag, 2018)

Creep, fatigue, and static tests were performed on a single lap shear test by Olivier et al. (2021). In this research, injected bolts were compared to iSRR connectors. The fatigue behaviour of the iSRR connectors proved to be far superior to the fatigue behaviour of injected bolts, as the iSRR connector could sustain 100x more stress cycles of $\pm 40kN$ (23.7 million vs 23.7 thousand cycles).

2.4.2. Wheel Loading

Wheel loading tests have been carried out on the iSRR connector by ter Kuile (2023). Both static and cyclic loading experiments were performed, as well as a numerical study based on FE-modelling in FEA-software Abaqus. Even though the iSRR connector was similar, the model that was tested differed slightly from the prior research by Csillag (2018). The research of focused on wheel loading tests only, instead of shear loading, and therefore used a slightly different iSRR connector concept as displayed in Figure 2.13 (FE-model).

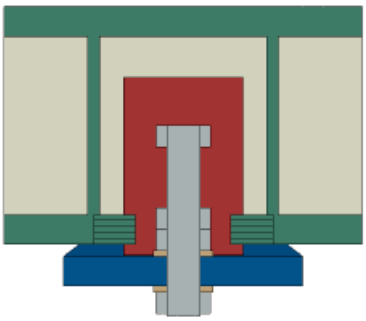

Figure 2.13: Model of the iSRR wheel loading connector (ter Kuile, 2023)

A purely static test resulted in a maximum load of 109kN (SP01). Here cracking in the foam core was observed until 50kN, after that a significant cracking sound allocated to delamination of the FRP bottom facing was heard at 85kN. Final failure occurred shortly after bending of the bottom facing. An additional

specimen (SP03) was first cyclically loaded for 1.77 million cycles at the loading range of 4.5kN to 45kN (R = 0.1, 4Hz). This specimen did not show significant damage, and was directly afterwards monotonically loaded in a static test until failure. Failure occurred at 123kN, with no significant cracking sounds indicating forms of failure until 108kN. Figure 2.14 shows the load displacement graph of both specimens.

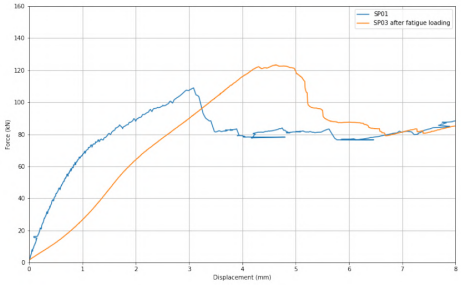

Figure 2.14: Load displacement graph for SP01 and Sp03 (ter Kuile, 2023)

The fatigue tests performed poorly, apart from SP03 with a loading range of 4.5kN-45kN. SP02 was loaded with a range of 10kN - 75kN (R = 0.13), and failed after 1600 cycles. The dominant failure mode observed was radial cracking of the iSRR ridge between the FRP and the steel plate, after which the connector punched through into the deck.

The numerical model was made in Abaqus, and made primarily use of the cohesive zone modelling method. The research concludes that the numerical model stems well with the experimental results, where the numerical modelling has the following features:

1. For the SRR a concrete damage plasticity model can be used.
2. The model made use of the Hashin damage criterion, in combination with the cohesive zone modelling method.
3. The interface behaviour between the FRP and iSRR is hard to predict, and it is suggested that more research is conducted to this aspect.
4. The initial stiffness, stiffness degradation and delamination stemmed well between the experiments and the numerical model.

Figure 2.15 shows both the numerical test results as well as the experimental test results. The experiments shows a more fluent stiffness degradation, where the numerical results are stockier. Final failure did however occur at almost the same load.

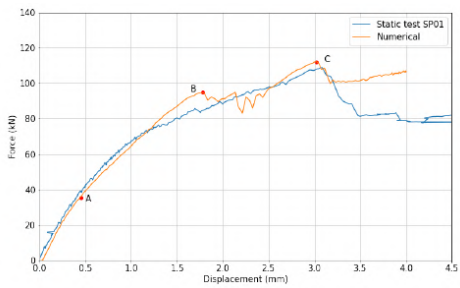

Figure 2.15: Numerical vs. experimental results (ter Kuile, 2023)

2.5. Conclusions

From each section the most important results, gaps in the research, or most useful information to use will be presented shortly in this section.

1. Vacuum infused panels take longer to be produced than pultruded panels, but have a much higher versatility in fibre direction, as well as good punching shear performance. Using Infracore Inside

technology also increases debonding strength of the foamcore to the FRP, making this a preferred combination for bridge decks sustaining hybrid interaction.

2. Many ways of creating composite/hybrid interaction exist, but blind-bolting seems the best way to make the system also demountable.
3. A common limitation of FRP-steel mechanical connectors is the initial stiffness. Injected bolts can provide more stiffness than standard blind-bolts, but creating composite interaction is still cumbersome. Injected bolts also excel at fatigue performance, as the fatigue life generally is 3 times longer than that of standard bolts.
4. The iSRR connector has a high initial stiffness, and is subject to current research. The most common failure modes are delamination of the bottom facing of the FRP due to bending, as well as radial cracking of the reinforced resin. The connector performs well in shear, with an ultimate loading capacity of 160kN. Also in cyclic shear tests the iSRR connector performs better than injected bolts, being able to sustain 100 times more stress cycles. Leading in the slip behaviour with respect to shear deformation is the deformation of the bolt, followed by crushing of the SRR.
5. The current iSRR connector designs are limited in their cyclic wheel loading resistance. A cyclic resistance of 1600 cycles is measured at the load range 10kN - 75kN.

3 Requirements

The goal of the new type of FRP-steel demountable connector is to be able to replace old bridge decks on steel superstructures with the FRP decks. The design of the connector will be subject to certain requirements, both in the form of expected vertical wheel loads and positional tolerances. Hence a case-study is chosen by the means of the bridge Nieuw-Vossemeer (Figure 3.1). This chapter covers the expected load-levels for the connector due to local wheel loading, as well as requirements regarding the execution tolerances.

The bridge Nieuw-Vossemeer spans 7 fields, of which the middle span is an arch bridge spanning 140m. The bridge was chosen specifically for the following reasons:

1. The spacing between girders is smaller than 3m (= 2.375m)
2. The deck lies on top of the steel girders.
3. The deck is made of concrete, connected by shear studs.
4. Composite behaviour only occurs in the longitudinal direction (driving direction), not in the lateral direction.

The bridge deck itself is supported on three main longitudinal girders (M1 - M3), two secondary longitudinal girders (S1 - S2) (see Figure 3.2a), and cross-girders spaced at maximum 8 meters apart. The cross-girders play no part in this case-study, as the connectors are modelled to be on the longitudinal girders only.

The case-study is meant as an indication into what load levels are expected for wheel loading only, shear forces are not analysed. It is possible to conduct a more in-depth analysis than the presented one here. However, the level of detail is chosen as the distribution of forces between different connectors due to the varying stiffness of the deck between the two main directions is of most interest.

3.1. Numerical Model

For the modelling Abaqus (Abaqus, n.d.) has been used. This is not necessarily the fastest type of software to work with due to its research nature, where the application here is just engineering oriented. However, the facilities of Abaqus to model laminates are one of the arguments to do use Abaqus for

Figure 3.1: Bridge Nieuw-Vossemeer (van der Heijden, 2023)

this analysis. The deck itself is fully modelled with shell elements, which have the laminate properties assigned to them by means of the Classical Laminate Theory. The laminate build up can be found in Appendix A.

Figure 3.2a displays a top view of the deck, where the shaded areas are not available to cars. 2 notional lanes remain, which are primarily supported over girder M2, M3, S1 and S2.

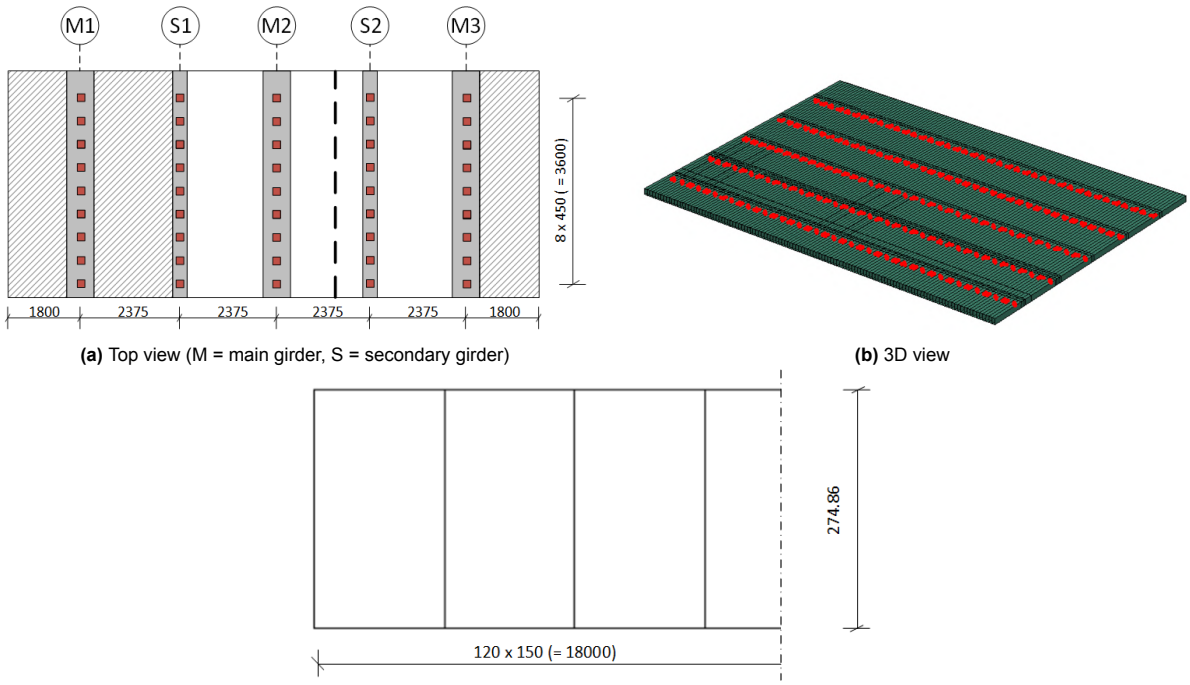

(a) Top view (M = main girder, S = secondary girder)

(b) 3D view

(c) Side view

Figure 3.2: Deck layout, with the location of the connectors indicated in red

The girders are not modelled, only the deck is. The girders are mimicked by application of the connectors after every third web, such that the connector spacing is 450mm. The connectors are modelled by boundary conditions on a square area of 150mm x 150mm, where all rotations are allowed for. Girder M2 is also restricted in all displacements, girders M1-M3 and S1-S2 are allowed to have transverse displacements. The latter mimics that the bridge does not have transverse composite interaction.

3.2. Loads - Ultimate Limit State

The Eurocode EN-1991-2 (NEN, 2021a) describes multiple load models (LM) able to be used for verifications. In the case of wheel loading on the connector local failure modes are to be assessed, such that only load models applicable to local verifications should be used. For the Ultimate Limit State the relevant load models are LM1 and LM2.

3.2.1. LM2

LM2 is the less complex loadmodel of LM1 and LM2, as it only makes use of one axle of 400kN. The area of the wheels is 350mm x 600mm, such that the wheel can drive almost over two connectors at the same time (connector spacing = 450mm). The highest load therefore occurs when the axle is on the same horizontal line as the connector, such that two loading cases remain, referred to as ”Case 1 - Connector in the middle of the axle”, and ”Case 2 - Wheel on connector”, as displayed in Figure 3.3.

The reaction forces under the overloaded connector are measured, and come out as:

1. LM2 Case 1: 187kN
2. LM2 Case 2: 188kN

Case 2 gives the highest reaction force, but is close in magnitude to Case 1. It is notable that the reaction force is lower than half the axle force. The close connector spacing and the relative small area

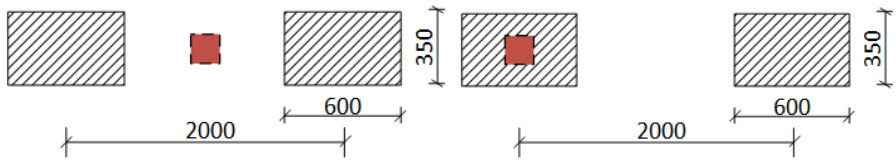

(a) Case 1 - Connector in the middle of the axle **(b)** Case 2 - Wheel on connector

Figure 3.3: Load cases for LM2

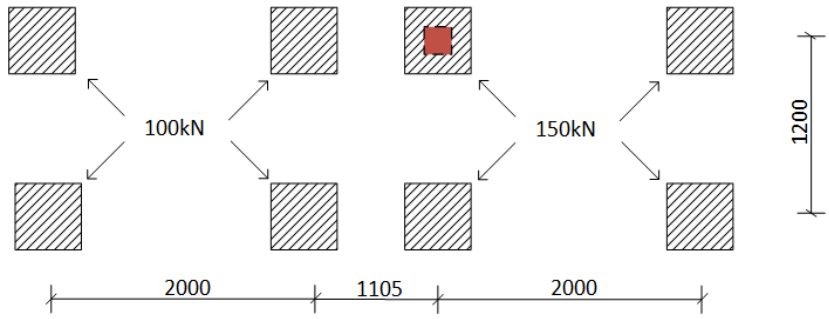

Figure 3.4: Load case for LM1

of the connector compared to the wheel make that the wheel hangs over the connector, resulting in reaction forces in adjacent connectors. Hence in applications the maximum expected value of 200kN will not be reached, but is about 7% lower.

3.2.2. LM1

LM1 covers the concentrated and uniformly distributed loads of standardized vehicles. The load model uses both axle loads and uniformly distributed loads, however for local verifications only the axle loads are taken into account. The axles have their loads defined as: $\alpha_Q \cdot Q_k$, with α_Q being the adjustment factor, and Q_k being the characteristic value of the axle load. The notional lane, lane 1, experiences axle loads of $Q_k = 300kN$, which is divided over 2 wheels. The adjustment factor depends per situation, but in case of more than 2 million trucks per year, the adjustment factor equals 1.0. The second lane experiences axle loads of 200kN. the axles are located on their own lanes, and are shifted to create maximum local loads on a connector, where the spacing between 2 vehicles should remain more than 500mm.

This wheel loading has to be applied over a representative wheel contact area of 400m x 400mm. Taking into account that Case 2 is normative in LM2, a similar case is modelled for LM1. The heaviest axle will have a wheel placed on a connector, the lower weight axle is placed as close to this connector as possible according to the Eurocode. The space between the axle sets is 1015mm (> 500mm), the limitation here comes from the placement of the lanes with respect to the girders. The placement of the wheels is displayed in Figure 3.4. The connector that is loaded maximally is highlighted, the loading applied is denoted per wheel.

The resulting force in the connector is 177kN. In contrast to LM2 it is seen that the resulting force in the connector is larger than the wheel loading applied directly on top of the connector. The wheelload directly on top of the connector still disperses to the other connectors due to the overhanging of the wheel, as the area 400mm x 400mm of the wheel is significantly larger than the area of 150mm x 150mm of the connector. However, other wheels of different axles are placed between girders, hence resulting in force being applied from these wheels to the connector that is tried to be overloaded as well.

3.3. Loads - Fatigue Limit State

Fatigue loading is important in bridge design, as repeated passing of trucks induces loadvarying cycles which are often of high importance on the design of details in bridges (Szerszen and Nowak, 2000). Fatigue behaviour of a material or detail is often characterized by S-N curves, curves denoting the

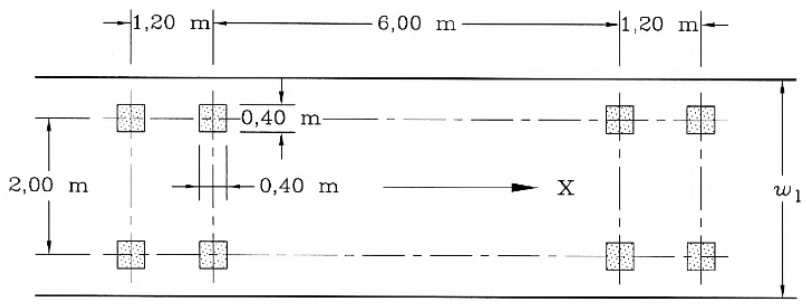

Figure 3.5: Fatigue Load Model 3 from EN1991-2 (NEN, 2021b)

expected amount of cycles (N) the structure can withstand at a certain stressranges (S). The latter refers to that not the reached loadlevel is of importance, but rather the difference between the lowest and the highest loadlevel in a cycle.

3.3.1. FLM3

Fatigue load model 3 (FLM3) will be used to determine the expected range in loadcycles on a connector. FLM3 is used for this since all axles are equally loaded, and hence irregularities in loading on a connector are easier to find. This loadmodel will only be used to see the influence of having multiple axles driving over a connector, and to see how the loadcycles should be counted.

Figure 3.5 shows the layout of the axles, where it can be seen that the axle spacing is only 1.2 meters between the axles in a set of 2, and has a spacing between two sets of two axles of 6 meters. Hence, two loadcases can be reasoned, 1. either the passing of each axle induces maximum loading, or 2. the passing of each set of axles induces the maximum load.

The same numerical model is used for FLM3 as is for LM1 and LM2. From LM1 and LM2 it is reasoned that the largest forces occur in a single connector when a wheel drives directly over this connector. Similar behaviour is found for FLM3, where the force for the passing of axle number one is as:

1. Wheel on girder: 56kN
2. Axle over girder: 54kN

The significant moments during the passing of a truck are modelled for the first case, and are plotted to create a loading diagram for one connector as a truck passes over the connector. The diagram is presented in Figure 3.6. It is seen that the force reaches 56kN when the wheel is directly on top of the connector, and drops down to 2kN when the connector falls exactly between the two 1.2m spaced axles. This effect is attributed to the close connector spacing (450mm), which is significantly smaller than the spacing between two axles (1200mm). The conclusion reads that for fatigue cycle counting the passing per axle should be taken into account separately, and that no reduction should be taken into account for the passing of groups of axles.

3.3.2. FLM4

FLM4 is the model that is actually of interest for bridge applications and is used to calculate the amount of expected high loadlevel cycles. The model is comprised of several standard trucks with specific dimensions and loads of axles, hence being more refined than FLM3. The national annex regarding traffic loads for the Netherlands NEN-EN 1991-2+C1/NA (NEN, 2021b) splits FLM4 in two separate cases, called FLM4a and FLM4b. Table NA.8 of that Eurocode Annex describes the truck models applicable for loadmodel FLM4b, which has heavier trucks added than model FLM4a. Hence in model FLM4b the heaviest axles are found in a single truck, which has 2 axles of 180kN and 170kN respectively. These axles are spaced 1400mm apart, of which each axle has dimensions as (with two wheelsets, of 2 wheels per wheelset):

1. Wheelset spacing = 2000mm
2. Wheelspacing in set = 320mm c.t.c.

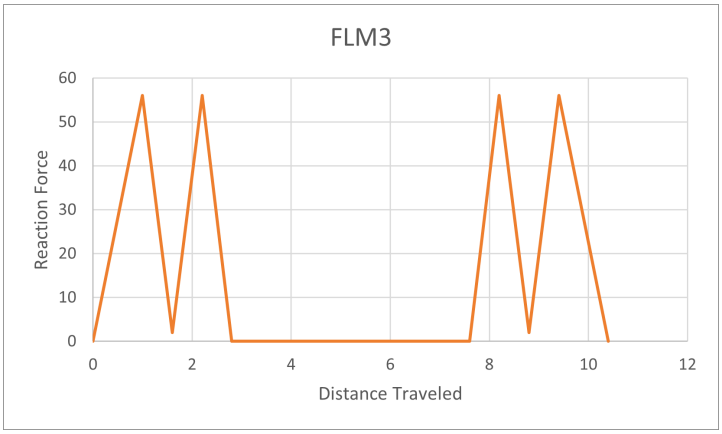

Figure 3.6: FLM3 - Loads per passing of a truck

Table 3.1: FLM4 results of different configurations

Situation	Axle Placement		170kN axle present?	Reaction Force Connector (kN)
	Wheel on girder	Axle over girder		
1	x	-	no	84.1
2	x	-	yes	84.3
3	-	x	no	85.0
4	-	x	yes	85.8

3. Wheel in wheelset = w x h = 220mm x 320mm

From the analysis of FLM3 it can be reasoned that the lateral placement of the axle exerts a minimal influence on the reaction force at the connector. Similarly, the addition of extra axles has almost no contribution to the reaction force either. To verify these trends, the configurations as in Table 3.1 are tested. The variables included are:

1. Lateral placement of the axle
2. Incorporation of supplementary 170kN axle (180kN is always present)

The addition of the 170kN axle has a small influence of approximately 0.6% on average. The placement of the axle laterally has different effects than in other models, as the placement of the axle symmetrically over the girder increases the reaction force with about 1.4% on average compared to one wheelset being exactly on top of the girder. The configuration of the wheelset is of influence here, as the wheelset consists of two smaller wheels, and has therefore more overhang over the connector than other loadmodels do.

3.4. Geometrical Requirements

The set of requirements for the connector from a geometrical point of view are given by tolerances during the execution stage of the project. Misalignments during assembly of the bridge can result from mistakes during the production stage of the individual components. Horizontal misalignment might result in that some bolts do not align with the bolt holes they are meant to fit in. Production tolerances of the FRP deck might result in angular misalignment of the deck with the steel girder, and waving of the bottom facing might occur. This section will briefly discuss the different requirements that need to be either designed or tested for.

3.4.1. Steel Girders - Oversized Holes

The bridge deck will consist of several panels with each of these panels having a certain amount of connectors pre-installed. If the pre-drilled holes in the steel girder have the same diameter as the bolts in the decks, the chances are very high that not all of the bolts of the bridge deck will fit into the holes of the steel girder. This could happen due to minor mistakes, e.g. the holes in the steel girder can be

Table 3.2: Nominal hole clearances, Table 11 from EN 1090-2 (NEN, 2021a)

Nominal Bolt Diameter (mm)	**12**	**14**	**16**	**18**	**20**	**22**	**24**	**27 to 36**
Normal round holes	1		2					3
Oversized round holes	3		4				6	8
Short slotted holes	4		6				8	10
Long slotted holes	1.5 x d							

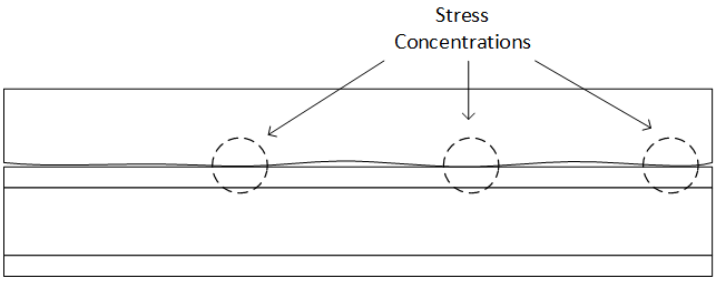

Figure 3.7: Stress concentrations due to waving of the bottom FRP facing

cut a millimeter to the side, the holes can be a bit too small, or due to settling of the reinforced resin in the connector, the bolt might have moved a little bit. These deviations are accounted for by enlarging the holes in the steel girder, creating oversized holes. EN 1090-2 (NEN, 2021a) covers the nominal clearances for bolt holes (Table 3.2), where the diameter of the bolt hole becomes:

$$d_h = d_b + nominal\ clearance \tag{3.1}$$

Nijgh and Veljkovic (2020) conducted a study regarding a carpark floor system, where a concrete floor with demountable shear connectors was placed on existing steel girders. The span of the steel beams was 14.4m, the individual floor slabs were 2.6m wide. To successfully fit the flooring system, significantly oversized holes of 12mm extra were needed for bolts grade M20. The research continued to show that generally a nominal hole clearance of 12.7mm to 22.6mm is needed for successful installation of such a flooring system. The case study performed by Nijgh et al was aimed at flooring systems in car parks, where the span (14.4m) is significantly smaller than for highway bridges. For this reason, it is chosen to apply a nominal hole clearance of 33mm, such that the total oversized hole diameter becomes:

$$d_h = d_b + nominalclearance = 27mm + 33mm = 60mm \tag{3.2}$$

3.4.2. Deck Clearance: Out-of-Straightness of the FRP Deck

The FRP decks that are used for the experiments are sandwich panels delivered by InfraCore. The panels are produced by the method of vacuum infusion, and make use of the earlier described InfraCore Inside waving pattern. During the production stage, and the subsequent assembly stage, it can occur that the FRP plies are not entirely straight. The out-of-straightness can occur globally due to an inadequate production process of the deck, where the webs are not entirely perpendicular to the flanges. Similarly waviness of the FRP flange can lead to local deformations. While this phenomenon may not significantly hinder the global resistance, it can result in unforeseen stress concentration during local verifications at the connection level which have not been accounted for in the design process. If it is assumed that the FRP-deck is flat and distributes the forces equally over the contact are with the beam, these deviations lead to premature failure of the bottom FRP plies, see Figure 3.7. The failure of these FRP plies on itself leads to loss of the pre-load force in the bolts if the FRP is contained in the clamping package. Furthermore localized failure in the facing can affect the resistance in shear bearing and bending of the flange. To bypass potential stress concentrations, a clearance of at least 10mm will be maintained between the FRP deck and the steel girder.

3.4.3. Angular Deviation

The perfect situation for a bridge deck involves parallel alignment with the main girder to which it is attached. In this ideal case the connector is produced in a straight manor, and hence no eccentricities occur, inducing imperfect behaviour. In reality the FRP decks will be mounted on pre-existing steel girders. This situation often leads to the tilting of flanges, thereby generating angular deviations between the connector and the bridge deck or steel flange. Many different types of deviations can be identified according to the Eurocode, and can be super-imposed on one another. A pending project at the TU Delft shows (preliminary) that this type of angular deviation can reach up to about 2 degrees, given that the influence length is taken as 3 meters (centre-to-centre distance of secondary girders).

3.5. Conclusions

This chapter is used to describe and lay down the boundary conditions for the design of the iSRR connector with respect to wheel loading. The conclusion can be laid down as a short and comprehensive list (Table 3.3), starting with the loads to sustain, followed by geometrical requirements of the connector:

Table 3.3: Comprehensive list of the design requirements

Type	Requirement
ULS	188kN
FLS	85kN - 500.000 cycles
D_{hole}	60mm
Deck Clearance	10mm
Angular Deviation	2 °

4

Numerical Analysis

This chapter covers the numerical modelling and the assessment of the different designs in the FEA-software Abaqus. First the global design concept will be explained, after which the variants of this design are elaborated upon. The FE-model will be described, including mesh elements, mesh size, material parameters, and interactions. A combination of quantitative and qualitative numerical assessments will result in a design most likely to succeed in experimental tests as a proof of concept.

4.1. Design Concept

As discussed in the former chapter, the design has to cope with a few boundary conditions. A vertical clearance needs to be kept, rotation needs to be allowed for, and the connection should be applicable in combination with oversized holes in the steel girder. As the connection has to deal with cyclic loading, creep of FRP occurs and can create a loss of the clamping force if FRP is contained in the clamping package ("ffm-technical-ffm981603-128", 2016). Starting with the last part, it is seen that the clamping package has to be fully made out of steel. This means for the design that the spacer to keep a vertical clearance also has to be made out of steel since it will be contained in the clamping package. Together with the requirement to allow for rotations, the vertical spacer will be a spherical steel plate, as showcased in Figure 4.1d and with dimensions in Appendix B.

All designs will have the same basic concept, with the shape and dimensions of the spherical steel plate being the variables. The basic design is showcased in Figure 4.1. Figure 4.1a displays a cross-section of the model. The concept of the former iSRR connectors remains, a bolt M27 10.9 is embedded in the FRP deck by means of injection with reinforced resin. The bolt has in total three embedded nuts, one at the bolt end and two at the level of the bottom of the reinforced resin. A washer separates these bolts from the spherical steel plate. Figure 4.1d displays the steel package, excluding the steel girder flange. This spherical plate is separated from the bottom FRP flange by a thin layer ($\approx 3mm$) of reinforced resin. This layer of reinforced resin is part of the embedded reinforced resin in the deck (Figure 4.1c), and results from overflowing of the resin after pushing the steel package inside. This interface layer of resin is beneficial, as it levels out any imperfections in the FRP bottom flange.

A few alterations are made to this spherical plate to assess the types of behaviour possible. The alterations are to limit the amount of steel usage and vary the stiffness of the plate, while keeping the basic gross dimensions of diameter and bolthole size. The main alternatives are:

1. SP20: The basic version of the spherical plate. The total height of the plate is 20mm, of which 10mm is cylindrical and 10mm is spherical. The diameter of the plate is 150mm.
2. SP15: The same spherical bottom as SP20, only the thickness of the cylindrical part of the plate reduces to 5mm. The total height of the plate becomes 15mm, reducing the stiffness of the plate.
3. CU20: The same outer dimensions as SP20, but with cut-outs to reduce the steel volume. The cut-outs are taken as four quarters, leaving two main stiffeners in the plate. The cut-outs are filled with reinforced resin, being an extension of the embedded reinforced resin in the deck.
4. PP20: A punched plate with a total height of 20mm. The thickness of the steel is everywhere 10mm, the remaining cavity in the plate is filled with reinforced resin. This design is offered for

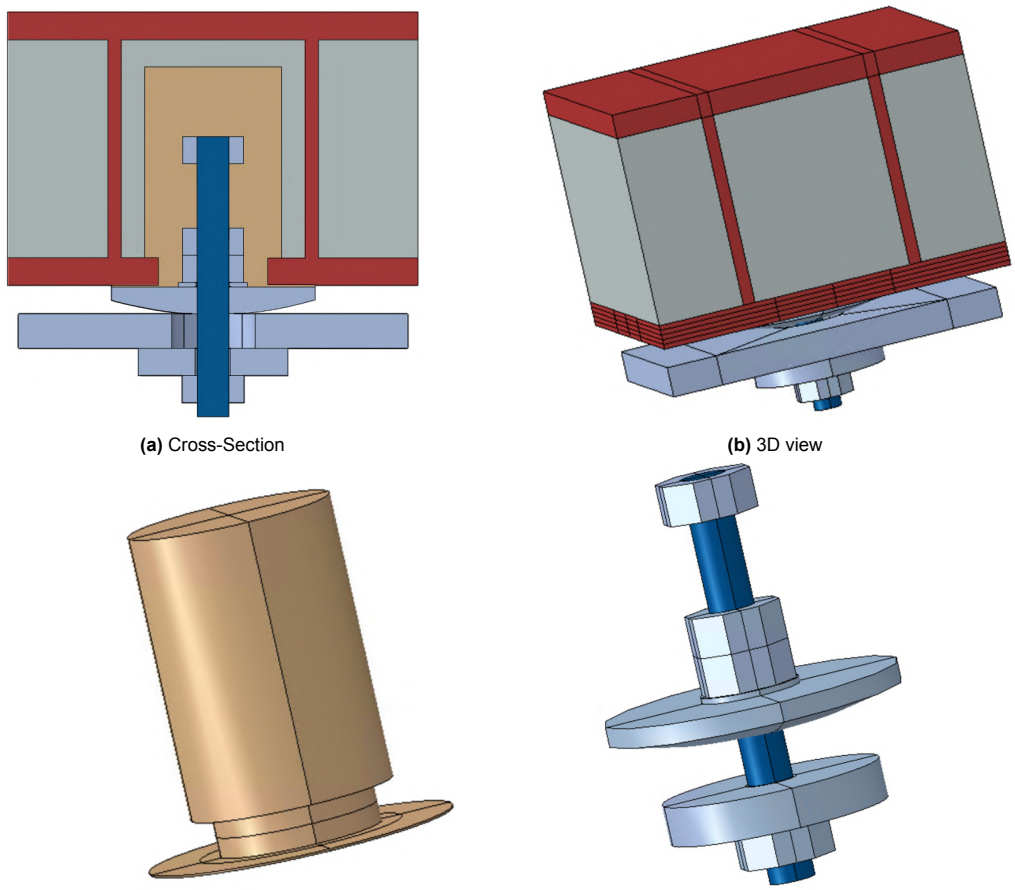

(a) Cross-Section **(b)** 3D view

(c) Injected reinforced resin **(d)** Steel package, excluding girder flange

Figure 4.1: Design concept

easier production. The former plates have to be made with CNC piece by piece. The punched plate can be produced by clamping all four edges, and pushing the centre of the plate downwards to create the sphere-like shape.

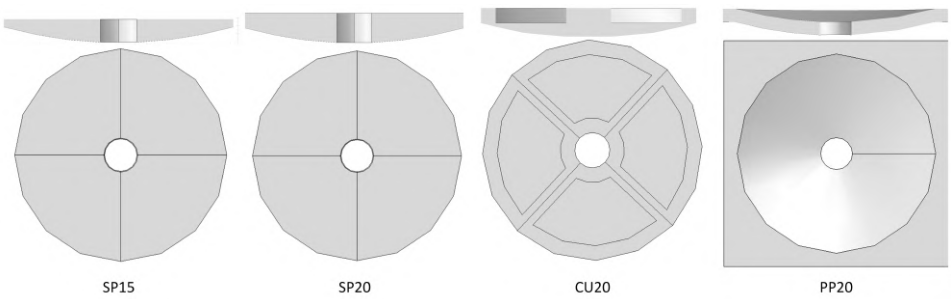

Figure 4.2: Concepts SP15, SP20, CU20 and PP20

4.2. Model Description

This section will give an overview of the input into the Finite Element Model used for the numerical analysis, again with the software Abaqus. It is important to note that the bolt diameter in the model (M23 10.9) differs from that of the design as will be used in practice (M27 10.9). This reduction of the diameter in the model is applied as the threads of the bolt are not modelled. It also follows that the

bolthole in the spherical steel plate is 24mm instead of 28mm, and that the washers and nuts are fitted to a boltdiameter of 23mm.

4.2.1. Material Models

The aim of the model is to find the ultimate resistance and the failure mechanisms associated with this resistance. As load concentrations and failure are only expected around the bolt hole, damage and plasticity properties are applied at critical locations. This entails mostly all parts associated with the bolt and the steel clamping package. In addition the bottom flange of the FRP will be modelled to include delamination by applying cohesive zones between five separate plies. In other parts of the model only the elastic properties are of importance, for example the webs and top flange of the FRP deck. The materials are defined based on former research regarding similar or exactly the same materials as used in this project. For exact deduction of the parameters references are made to Csillag (2018) and ter Kuile (2023). The following materials are defined (the exact parameters are listed in Appendix A):

1. FRP general: General FRP linear elastic properties are assigned to the webs and the top flange of the FRP deck. Failure is not expected in these areas, such that non-linear properties are not assigned in order to keep computation time low. The laminate build up can also be found in Appendix A.
2. FRP bottom flange: This area is expected to be prone to failure on a laminate level as well as on an interlaminate level. The bottom flange is subdivided in five stacked sublaminates, each having a cohesive interface with its adjacent laminates. The cohesive interfaces are able to capture delamination in the form of cohesive damage. Hashin damage properties are assigned to the sublaminates.
3. Reinforced resin: As opposed to normal resin, reinforced resin is not homogeneous. Due to the embedded steel shot concrete damage models characterize the material well (ter Kuile, 2023). Both tensile and compressive stress and damage can occur around the bolt, which properties are based on tests conducted on Daron 8151 resin and S390-HRC 40-50 steel shot (Christoforidou et al., 2023).
4. Foam: The core is made of a crushable PUR-like foam. The plasticity model in Abaqus for crushable-foam is applied in combination with foam hardening.
5. Steel: The steel in the spherical plate, bolts, nuts, and the baseplate is assigned as linear elastic with standard parameters for S355 steel.

4.2.2. Loading and Boundary Conditions

The analysis of the model is set up in 3 steps; the initiation step, the preloading step, and the loading step. During the initiation step the boundary conditions are applied to fix the model in place, and are in line with the experimental tests as will be performed later. The restriction in movement is applied at the short sides of the steel girder plate, where both edges are clamped. Hence all displacements and rotations are restricted.

The second step is where the preloading is applied to the bolt. Preloading in bolts can be applied by either modelling a direct load in the bolt, or by shrinkage due to a temperature field in the bolt. The latter has a shorter computation time and avoids the chance of singularities (Krolo et al., 2016), such that the predefined field is the preferred method. The predefined field is applied to the part of the bolt between the lower two nuts. The magnitude in Abaqus of -6500 yields a preloading force of 281kN, which is formed with a smooth step of 50s.

The last step covers the boundary conditions that are applied during the loading of the analysis. To simulate the wheel loading, a deformation is applied at the top of the FRP deck. The deformation is uniform over an area of 200mm x 200mm placed symmetrically 50mm from each edge. The given deformation of 20mm is exerted on the block with a smooth step of 3600s.

4.2.3. Interactions

The different parts of the model all interact in one way or another together. The most general type of friction contact is applied to each set of interacting parts, constituting of two types of behaviour:

1. Normal Behaviour: Hard contact is defined in the pressure-overclosure and the constraint enforcement method, minimizing penetration of surfaces (Abaqus, n.d.).
2. Tangential Behaviour: A penalty with general friction coefficient $\mu = 0.2$ (Csillag, 2018) is applied isotropically.

Table 4.1 lists the specific interactions that are modelled to overrule the standard friction-like interaction. Cohesive interfaces are modelled between FRP sublaminates and in later models between FRP, reinforced resin and steel. The cohesive behaviour here is based on the default settings of Abaqus Explicit. Furthermore damage initiation and evolution parameters are set, which can be found in Appendix A. The bolt and its nuts normally are screwed onto each other, but as mentioned in this model the bolt thread is not modelled. To overcome this the surfaces of the nuts and the respective bolt areas are tied together.

During production the fibres are wrapped around the foam core, which is modelled by a tie constraint between the foam and the FRP deck. This in reality will at some point separate from each other, but little is known of this interaction. Since also this interaction is not expected to have a lot of influence on the model behaviour, a tie constraint is assumed to be sufficient.

Table 4.1: Applied interactions in the FE-model

Element 1	Element 2	Interaction
FRP sublaminate	FRP sublaminate	Cohesive Surface
Reinforced Resin Ring	Bottom FRP Deck	Cohesive Surface
Reinforced Resin Ring	Steel Spherical Plate	Cohesive Surface
Bolt Rod	Bolt Head	Tie
Bolt Rod	Nuts	Tie
FRP Deck	Foamcore	Tie
Injected Reinforced Resin	Reinforced Resin Ring	Tie

4.2.4. Mesh

The mesh applied depends on the level of accuracy expected or desired from that certain part in the model. The areas of interest for the analysis are all those parts expected to take part in the failure mechanisms or general behaviour of the model. Each part will be addressed separately to discuss mesh sizes and the used element types.

1. Reinforced resin (Figure 4.3e). High accuracy around the iSRR ring is needed to capture tension damage. To match the complex shape of the area linear tetrahedron elements of the type C3D4 are used, which are 3D stress elements.
2. Bolt rod (Figure 4.3d). The bolt rod needs an increased accuracy regarding the preload force which is captured in the bolt rod. Since also bending is to be captured, 4mm C3D10M elements are used, which are quadratic 3D stress tetrahedons.
3. Head, nuts and coverplate (Figure 4.3d). These parts are modelled with 8-noded brick elements, with reduced integration (C3D8R) to save computational time. The mesh size is 5mm for the coverplate and 4mm for the other parts.
4. Spherical steel plate (Figure 4.3c). Since this part is of primary interest in the research, and since bending will be of high importance again the C3D10M elements are used. To capture a high accuracy a mesh size of 7mm is applied. Note that this size occurs at the outside the plate, and reduces inwards due to convergence towards the bolthole.
5. Sublaminates (Figure 4.3f). The bottom facing is divided into five sublaminates to capture cohesive behaviour between those plies. A general purpose continuum shell element is of the type SC8R, with a meshsize of 10mm.
6. FRP deck, excluding bottom facing (Figure 4.3a). Again the SC8R element is used, with also an element size of 10mm. The thickness of the webs and the topfacing is however not divided into multiple plies, as delamination is not expected to occur in these areas.

7. Foamcore (Figure 4.3a). Elements of the type C3D8R are used, as damage models of the concrete type are embedded in the material properties. The foamcore is not of a high importance and contains the largest volume of all the parts, hence it has a large meshsize of 12mm.

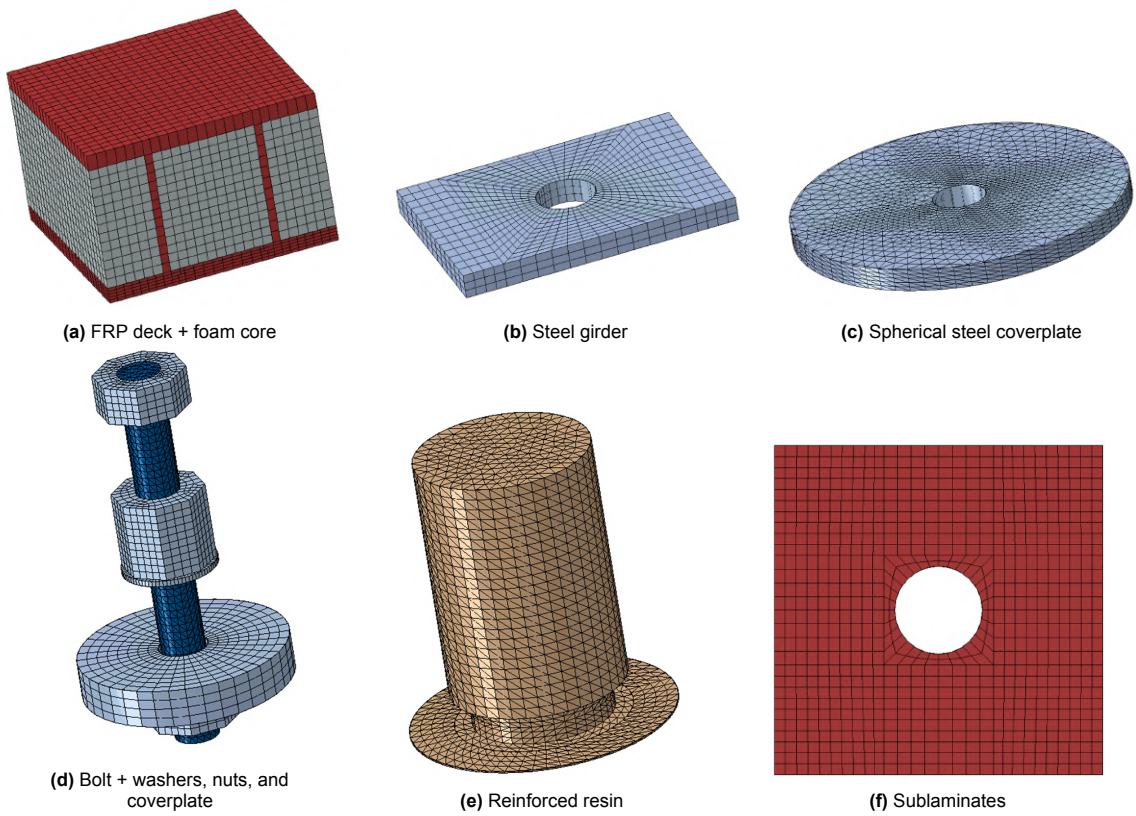

(a) FRP deck + foam core **(b)** Steel girder **(c)** Spherical steel coverplate

(d) Bolt + washers, nuts, and coverplate **(e)** Reinforced resin **(f)** Sublaminates

Figure 4.3: The mesh of all instances of the model

4.3. Resistance and Behaviour of the Alternatives

The different designs have been modelled and their ultimate resistances are calculated in Abaqus, resulting in the four load-displacement curves in Figure 4.4. This section will briefly describe the behaviour of each separate alternative, after which a design is chosen to continue the analyses and experimental campaign with.

4.3.1. SP15

The plate SP15 has an ultimate resistance of 476kN. The plate has a similar initial stiffness to the alternatives CU20 and PP20, but stiffness degradation starts earlier. The degradation of stiffness originates from yielding in the spherical coverplate as a result from bending. Tensile stresses reach the yielding level of 355MPa earlier than in alternatives SP20 and CU20, simply because the second moment of inertia is smaller than that of the other alternatives. The ultimate resistance is governed by delamination of the bottom flange of the FRP. Since this failure mode is similar to the other connectors, a similar ultimate resistance is found.

After failure the resistance drops to about 250kN, at which level the resistance starts increasing again. This is for a short part due to regained strength as the bottom facing did not delaminate fully. The most resistance is however gained from extreme bending of the steel plate, creating a direct contact between the FRP deck and the steel girder.

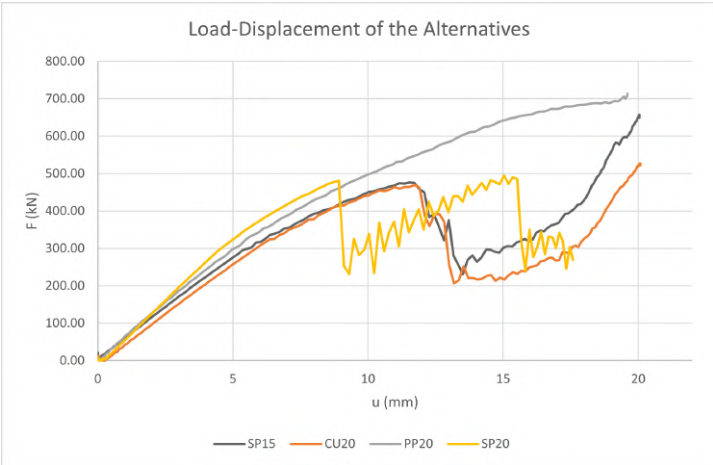

Figure 4.4: Load-displacement graphs of the different alternatives

4.3.2. SP20

The SP20 model has the highest stiffness of the four alternatives, and has the second highest resistance at 480kN. The higher resistance originates from the stiffness of the steel plate. More steel is used than in the other alternatives, creating a stiff steel spacer between the steel girder and the FRP deck. The result is a high initial stiffness with little yielding from the steel plate. The FRP flange is forced to bend around the spherical coverplate, due to the high stiffness of the latter. The bending of the FRP is related to the onset of delamination in the bottom flange of the FRP.

The decrease of stiffness in the connection is related to a combination of starting delamination and bending of the spherical coverplate.

4.3.3. CU20

The design of CU20 is similar to that of SP20, except that it has cutouts in the plate to reduce the amount of steel used. This reduction of steel usage lowers the stiffness of the connector, and creates a similar behaviour pattern to that of the SP15 plate. The result is a plate with two stiffeners which have to transfer most of the tensile stress resulting from bending of the plate. The plate can be accidentally rotated during production, hence it is important to verify its behaviour in both the standard and rotated case. The graph in Figure 4.5b shows the load-displacement curve for the plate with its stiffeners in the basic case, and for a 45 ° rotation (the situational sketch is presented in Figure 4.5a).

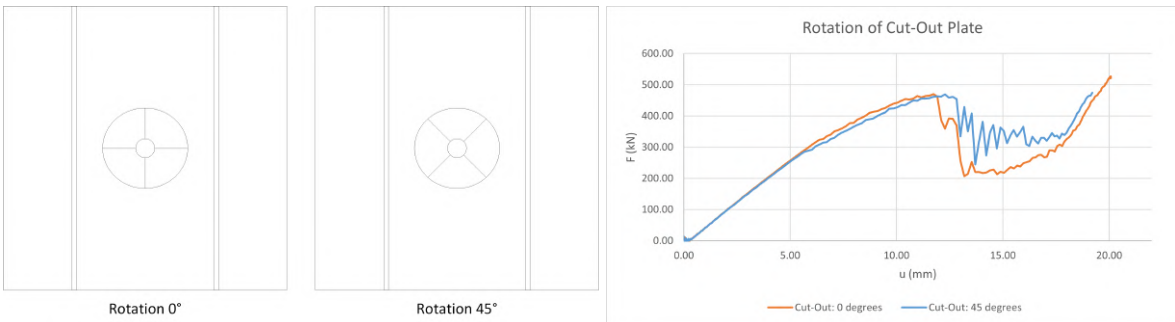

(a) Orientation of plate rotations

(b) Load-displacement graph of rotated plate CU20

Figure 4.5: Comparison between rotations of CU20 plate

The load displacement curve of both tests have the same initial stiffness. At approximately 280kN the stiffness of the 45° rotated plate starts decreasing with regards to the 0° plate. The 0° plate has one of the stiffeners in the primary axis of bending, creating a small increase in stiffness over the 45° plate. The difference is however small and the ultimate resistance is equal at 469kN. The ultimate failure mode is again delamination in the bottom flange of the FRP.

After failure the strength of the connection decreases, but regains a strength higher than the failure resistance at a deformation of about 20mm. This regained strength originates from extreme bending of the steel plate, allowing the FRP deck to have direct contact with the steel girder flange.

4.3.4. PP20

The PP20 plate seems to have the largest resistance from all the alternatives according to the load-displacement graph. The resistance keeps increasing, until delamination failure occurs at 712kN. Even though the ultimate resistance is high, the stiffness degradation is rather rapid. This stiffness degradation occurs due to the yielding of the steel plate, occurring immediately from the start. Figure 4.6 shows the local displacements around the steel plate at a loadlevel of 523kN, where the deformation of the steel plate is clearly visible. The steel plate bends so much even, that the edges of the plate come in contact with the steel girder. This creates a direct load path from the FRP-web, through the steel plate, to the steel girder, by pure compression. The delamination therefore occurs a lot later than in the other alternatives, as the lower flange is forced to bend around the steel plate a lot later than in the former alternatives, where the steel plate remains its shape.

The bending of the steel plate forces the reinforced resin inside to also bend. This leads to tensile stresses, which could become problematic during cyclic loading. The bending of the plate is significant enough to initiate cracking in the iSRR at an applied force of 90kN, see Figure 4.7.

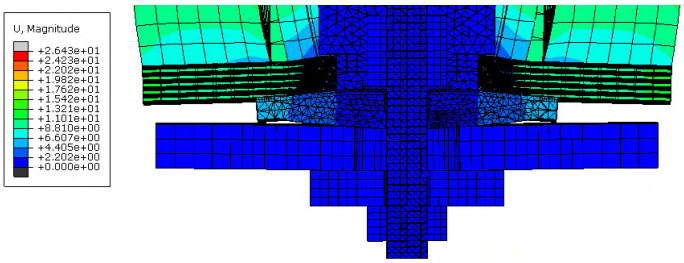

Figure 4.6: Displacement of PP20 at 523kN

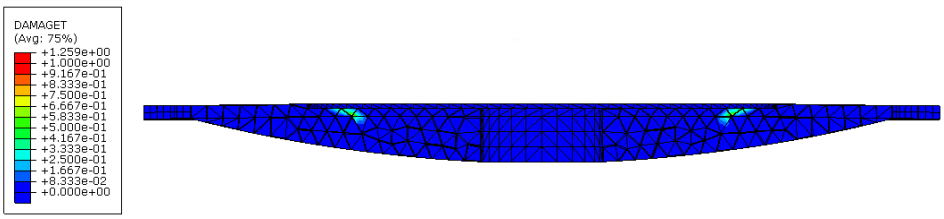

Figure 4.7: Crack initiation in iSRR at 90kN

4.3.5. Choice of alternative

Of these plates the most promising alternative is chosen to do the rest of the analyses and tests with. The ultimate resistance of the alternatives all exceeded the expected maximum amount from the Eurocode of 188kN, as reasoned in Section 3.2. With that reasoning, all the concepts presented suffice to do the static tests with. However, cyclic tests are also part of the test campaign, and are harder to predict. That, together with that this project is a proof of concept, are reasons that it is regarded wise to overshoot the resistance rather than to undershoot it. May the resistance be too high, then the optimum can be found in the future by adjusting the spherical coverplate.

Concept PP20 suffers from crack initiation at a loadlevel of 90kN, deeming the alternative not sufficient during cyclic loading.

Plates SP15, SP20 and CU20 have a similar ultimate resistance, but a higher stiffness is observed with plate SP20. Also stiffness degradation occurs later than in plates SP15 and CU20, such that SP20 seems to be the superior alternative over the other plates. The project continues with the plate SP20. This does not mean that the other plates are ruled out to be viable alternatives, but just that plate SP20 has the highest chance of succeeding.

4.3.6. Conclusion

The aim of this chapter was to conclude which alternative would be the most successful during the experimental campaign. Four different types of steel spherical plates are presented, which vary in stiffness and production methods. The FE-model used is presented, most importantly making use of a combination of CLT-modelling and cohesive zone modelling, where the latter is applied in the bottom flange of the FRP to capture cohesive damage and delamination.

Of the four alternatives concept SP20 was chosen to continue the testing campaign with. The main reasons are that loss of stiffness occurred the latest for this alternative, and had simultaneously the highest resistance combined with the lowest loss of stiffness (CU20 = 469kN; SP15 = 476kN; SP20 = 480kN; PP20 = 712kN). Other alternatives either had a lower stiffness (CU20/PP20/SP15), lower resistance (CU20/SP15), or early initiations of cracking in the iSRR being harmful to the cyclic resistance of the connection (PP20).

5

Numerical Analysis of SP20

In the former section concept SP20 has been deemed the design to pursue further analyses and experiments with. As an attempt to validate the usability of this design in real bridge applications, the design will be subjected to the geometrical deviations as described in Section 3.4. This chapter will present more in-depth results from the numerical testing of the standard case for concept SP20, and will analyse the behaviour of the connector in the following circumstances:

1. a 2° rotation of the steel girder flange with respect to the FRP deck.
2. a misalignment between the bridge deck and the girder flange, resulting in the bolt being off-centered in the oversized hole of the girder flange.

Furthermore in bridge applications the connection will be subjected to shear forces, where a preload force in the bolt is supposed to minimize slipping within the oversized hole. Hence in addition the preload force will be modelled and analysed in the standard geometry, and will in a later chapter be verified with results from the experimental campaign.

5.1. SP20 - Standard Situation

First of all the model for SP20 is refined by adding cohesive zones between the steel plate, the iSRR layer, and the bottom of the FRP flange. Sliding and gap openings between the steel spherical plate, the iSRR layer and the bottom FRP flange require therefore higher stresses to open up, increasing the resistance of the overall connection. The renewed load displacement graph is displayed in Figure 5.1. It can be seen that the ultimate resistance of the connection increases to 498kN, but that the stiffness remains similar.

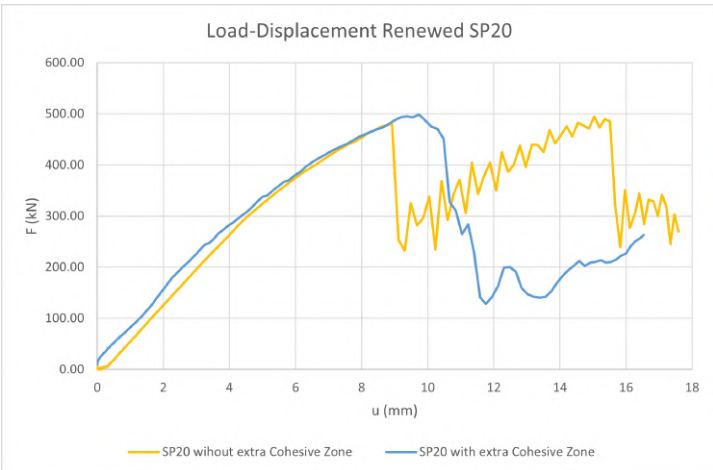

Figure 5.1: Load-displacement graph of renewed SP20 model

5.1.1. Failure Mechanism

The first indication of damage occurs at 250kN, the point at which the stiffness suddenly decreases a little bit. This moment coincides with the onset of separation of the iSRR ring and the bottom of the FRP flange. This delamination separation is initiated at around 102kN, and continues to increase in area size until around 360kN. After this moment the possible transfer of shear stresses in this area is almost fully reduced. Figure 5.2 displays the measure for cohesive damage at this interface area. The initiation of the strength reduction starts around 102kN with light damage (Figure 5.2a displays the cohesive damage at the bottom facing of the FRP). At around 218kN the first separation starts, which reaches its maximum at a loadlevel of 366kN. Figure 5.2b shows the cohesive damage at the top of the iSRR ring. The top of the ring shows that the sides of the iSRR at the location of the FRP webs suffer the most. These are after all the places where the bending is maximum. In addition the center between the webs bends the least and hence transfers the lowest shear stresses of this interface area. This area therefore also has the lowest cohesive damage, as is seen by the blue indicated patches close to the center of the iSRR.

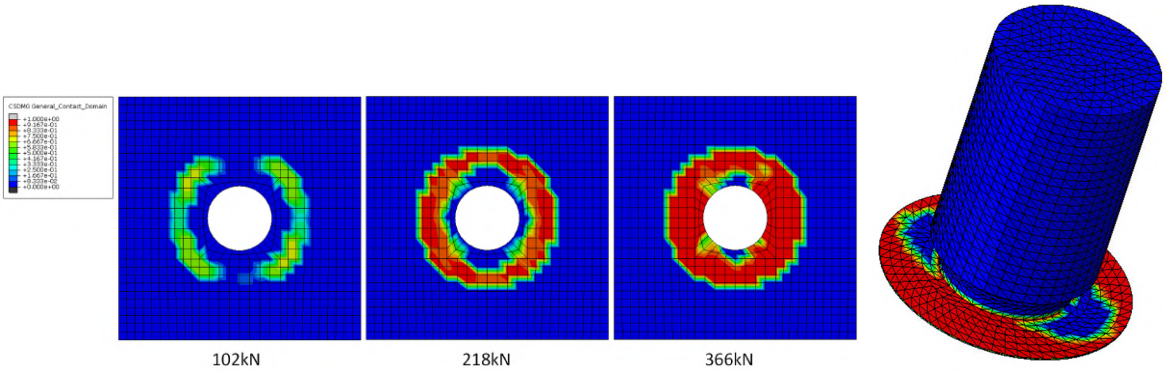

(a) Bottom FRP flange **(b)** iSRR (366kN)

Figure 5.2: Separation between the FRP flange and iSRR layer

Between loadlevel 250kN and 350kN the stiffness remains approximately similar, after which the stiffness starts decreasing until the point of failure. This stiffness reduction is attributed to delamination in the bottom facing of the FRP due to bending. This delamination is also measured in cohesive damage, and is maximum at the bottom of ply 3 (out of 5), closest to the bottom of the FRP deck. Figure 5.3 displays the progression of delamination, starting at 366kN. The onset of delamination coincides with the end of the cohesive damage propagation in the iSRR layer as described before. The initiation of delamination due to bending is delayed by the new cohesive interaction at the iSRR layer, creating a slightly higher resistance than in the former model.

The pattern of delamination is mostly contained between the webs of the FRP deck, which are located at the vertical damage patterns at the level of 498kN in Figure 5.3. The bending of the FRP is maximum around this location, as the compression force travels mostly through the webs. The FRP deck is free to deform (no restrictions are applied), hence limited bending occurs outside the webs of the FRP deck, and delamination is mostly contained within. The pattern of delamination is seen to be diagonal in the less concentrated areas. This is likely a result from hourglass problems.

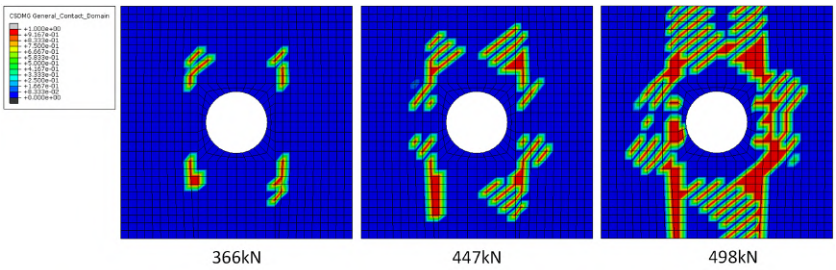

Figure 5.3: Delamination at the middle of the FRP flange (bottom ply 3)

5.1.2. Preload Force

In bridge applications the connection will have to transfer shear forces through friction. This friction force is a resultant of a preloading force in the bolt. Compressing the deck from the top will have influences on the magnitude of the preloading force, and likely could reduce it. By compression the length of the clamping package can reduce, resulting in a loss of preload force.

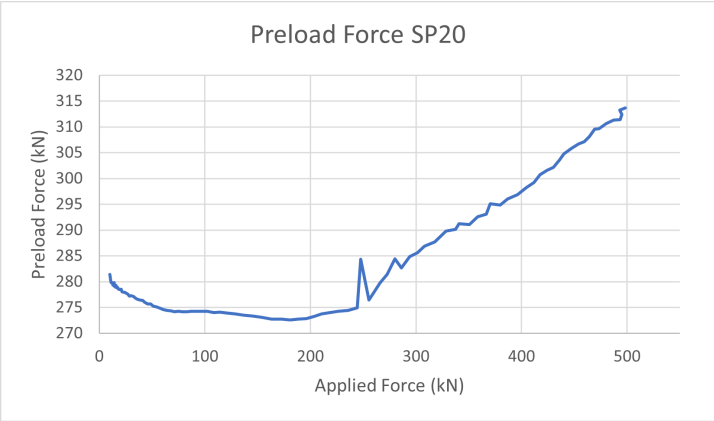

Figure 5.4: Preload force vs. applied load on SP20

In the model the preload force is applied between the two lower nuts. Applying a negative temperature field to this section of the bolt makes the bolt wanting to shrink. The other parts of the steel do not shrink, as these stay at normal temperature and hence do not deform. As the bolt shrinks and therefore moves the nuts closer together (a tie constraint is applied between the bolt and nuts), the nuts find resistance by the steel plates in between. The bolt tries to shrink more, but is restricted in movement, and hence creates a clamping force between its nuts. The initial preloading force generated is 281kN. The preload force graph can be seen in Figure 5.4, where the preload force is plotted on the y-axis, and the compression force applied at the top is plotted on the x-axis.

The preload force reduces as expected during the first part of the simulation, until an applied load level of 172kN. The preload force reduces during this period with 3.2% from 281kN to 272kN. After this moment the preload force starts increasing gradually, until it increases with a spike from 275kN to 284kN at an applied loadlevel of 244kN.

The sudden increase in preload force occurs simultaneously with full tensile damage in the iSRR ring (Figure 5.5). Due to cracking in the iSRR ring the bolt and the embedded iSRR are now free to punch through the deck, but is limited by the amount of bending of the steel spherical plate. The gap opening creates the possibility for elongation of the bolt, as tensile stresses are seen developing in stage 3 of Figure 5.6. The result is that the tensile stresses increase in the bolt, therefore also increasing the magnitude of the preload force. In reality however these numbers after failure have little meaning, as the clamping package is not continuous anymore.

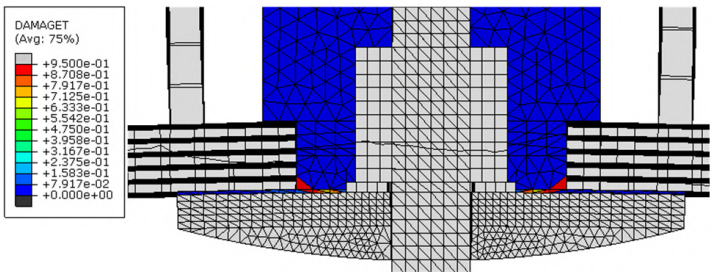

Figure 5.5: Tensile damage in iSRR

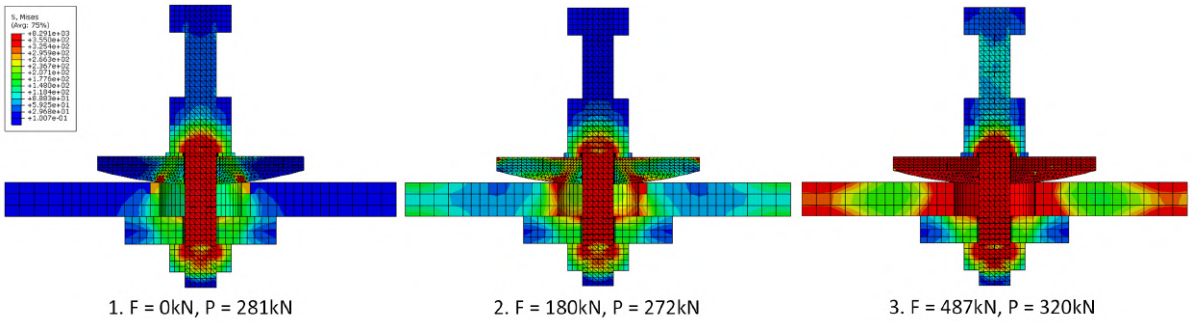

Figure 5.6: Progression of Von-Mises stresses in the clamping package

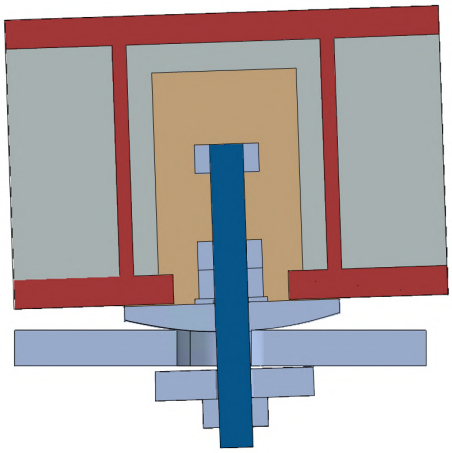

Figure 5.7: Cross-section the FE-model with a 2° rotation

5.2. Angular Deviation

Figure 5.7 displays the cross-section of the Abaqus model used for the simulation of the angular deviation. The steel girder remains in position, all other components are rotated. The benefit of the spherical coverplate can be seen, as the spherical plate remains in contact with the edges of the oversized bolt hole. The ordinary coverplate does not remain fully in contact with the steel girder. During shear loading this would reduce the slip area of the coverplate, resulting in a smaller friction force. A solution would need to be found for that specific case. The loadpath from the compression at the top however remains unaffected, except that the pre-loading package is not closed anymore due to the gap at the coverplate. The preload force therefore hardly develops, mostly resulting in very localized stresses at the nuts, which are subjected to bending.

A vertical deformation is induced at the top over the same 200mm x 200mm area as in the other simulations. The deformation occurs in the global vertical direction and hence has an eccentricity towards the bolt rod, possibly creating a bending moment in the bolt rod.

The load-displacement graph in Figure 5.8 shows that the ultimate resistance equals 434kN, with an initial stiffness of 69kN/mm.

Most apparent in the load-displacement graph is that the drop in force after the failure at 434kN is relatively small, dropping with 13.6% to 375kN. Thereafter the resistance builds up again until failure again occurs at 385kN. The two moments of failure are originating from the asymmetric nature of the 2° rotated block. Figure 5.9 shows that indeed also the failure mechanism is asymmetric. The left-hand side fails first, after which the right-hand side fails, both by means of delamination.

Figure 5.10 displays the progression of stresses in the steel package and the delamination in ply 2 out of 5 closest to the top of the bottom FRP flange. The spherical steel plate (Figure 5.10a) has two different lengths of leverarms with respect to the steel base plate, due to the rotation of the connector. The left-hand side has a shorter leverarm than the right-hand side, such that the spherical steel plate has a higher stiffness on the left-hand side than the right-hand side. Since the entire connector still has

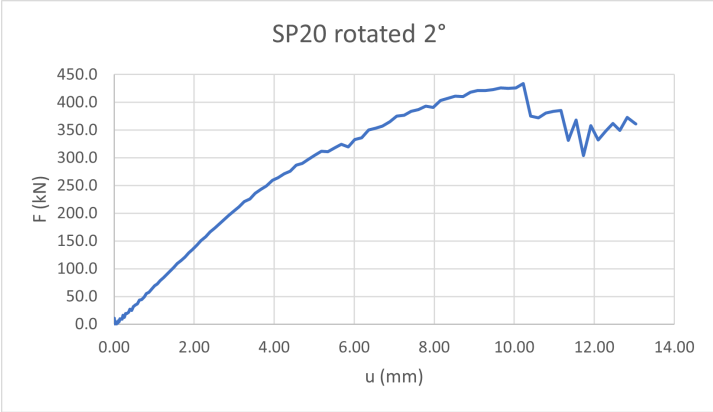

Figure 5.8: Load-displacement graph of SP20, with an added rotation of 2°

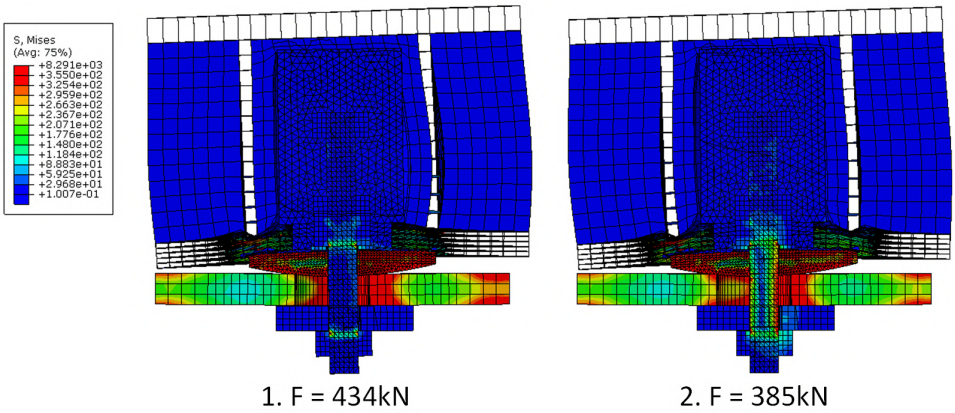

Figure 5.9: Cross-section at the two points of failure

to deform as one, and hence has the same stiffness, both sides of the connector work differently. The left-hand side has a higher stiffness in the steel, such that the deformation has to come from bending of the FRP. The right-hand side has a lower stiffness in the steel, such that the total deformation more governed by the bending of the steel coverplate. As such, at the same loadlevel the left-hand side experiences more bending in the FRP, such that delamination occurs earlier at that side. After this side fails due to delamination, the other side shortly follows. Figure 5.10b shows at failure point 1 that on both sides of the connector delamination is initiated, but that the left-hand side already is fully delaminated. At failure point 2 it is seen that the left-hand side remains in the same state, only the delamination of the right-hand side progresses further.

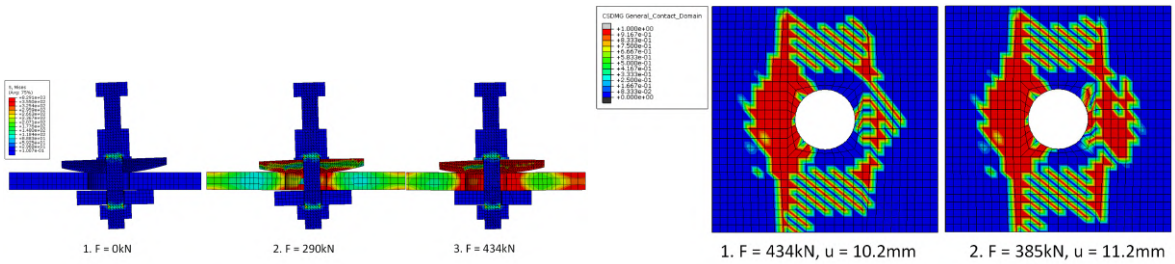

(a) Von-Mises stresses in the steel package

(b) Delamination at ply 2

Figure 5.10: Asymmetric failure modes at angular deviations

5.3. Off-Centered Placement

The oversized holes are used in the bridge girder to account for errors in the alignment of the bolt in the deck and the bolthole in the bridge girder. In the most standard scenario the bolt aligns with the centre of the hole, but this will as mentioned not always be the case. In the extreme case the bolt is placed fully off-centered, all the way at the edge of the bolt hole.

To simulate this the bridge deck, with the bolt and coverplate, is moved sideways to align the bolt with the edge of the hole (see Figure 5.11). An extra constraint is added in the model to prevent the block from slipping sideways to the centre. After all, in reality this movement would be restrained by the other bolts aligned in their respective holes. This boundary condition is applied at the sides of the bottom flange of the FRP, and only restrains horizontal movement.

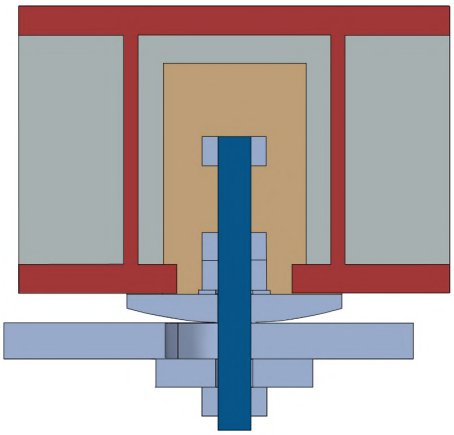

Figure 5.11: Cross-section of the FE-model with off-centered placement

The ultimate resistance of the model in the off-centered situation is 406kN (see Figure 5.12a). This resistance is lower than both the standard and 2° rotation situation. The initial stiffness is 67.8kN/mm. After the ultimate load at 406kN the analysis aborted due to not being able to converge to a solution within the set time step.

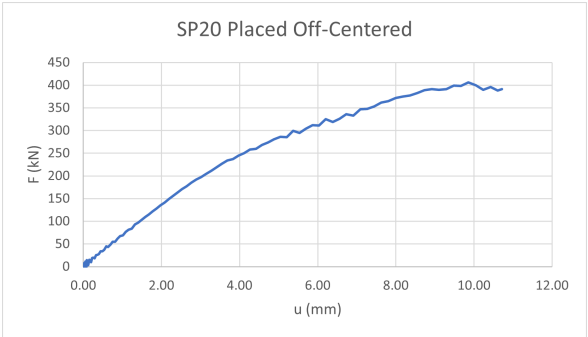

(a) Load-displacement graph

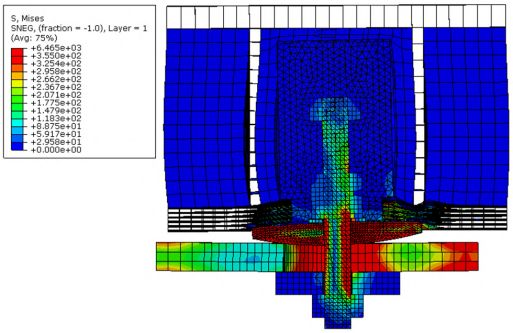

(b) Von-Mises stresses at ultimate failure

Figure 5.12: Off-centered SP20 results

Figure 5.12b displays the cross-section of the model at failure (406kN). It can be seen that only on one side of the bolt delamination occurred in the FRP, an asymmetric failure mode similar to the model with the angular deviation. The reason is in essence similar, namely that due to asymmetric placement the bending moments occurring in the spherical steel plate differ on both sides of the bolt. At a loadlevel of 0kN the right-hand side has the smaller leverarm, as it is supported by the steel baseplate. The left-hand side hangs fully free without a point of support, hence acting as a cantilever. Figure 5.13a displays that the left-hand side of the spherical steel plate experiences more deflection than the right-hand side. Again the connector experiences the same induced deflection, such that the combination of parts on both sides have to lead to the same total deflection. Since the left-hand side's steel plate bends more, the FRP has to compensate on the right-hand side by bending more than on the left-hand side. The

result is seen in Figure 5.13b, where full delamination is reached earlier on the right-hand side than on the left-hand side.

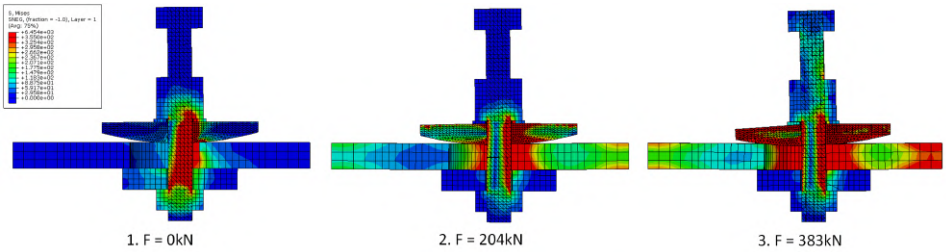

(a) Von Mises stresses in the steel package

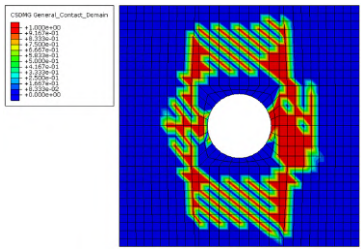

(b) Delamination in ply 2

Figure 5.13: Asymmetric failure modes due to off-centered placement

Figure 5.13a also shows the progression of preload stresses in the bolt. Opposed to the situation with angular deviations, this model is able to reach an expected preload stress pattern. By off-centering the bolt, only steel to steel contact is made at the side where the bolt is placed at. The result is an asymmetric loading pattern as seen in step 1, where all the compressive forces are transferred through one side of the steel flange only. The following two loadsteps, 204kN and 383kN, show the same preload pattern between the two lowest nuts. Stresses are maximum at both sides of the bolt, and reach at some point 0MPa close to the centre line of the bolt. This pattern of stresses is affiliated with bending of the bolt, resulting from the free space under the left-hand side of the spherical steel plate. As the spherical plate has a bolthole with a diameter of 1mm larger than the bolt, the plate is able to rotate a little bit, inducing the bending stresses as seen in the bolt. At point 2 it is seen that the bending stresses only occur in the preloading package, close to failure at point 3 the stresses also develop outside the preloading package. This is for the same reason as for the basic scenario as mentioned in Section 5.1.2.

5.4. Conclusions

The aim of this section was to perform a more in-depth analysis on the design of SP20 regarding geometrical deviations and preload forces in the bolt. An improved FE-model is used, where additional cohesive interactions are added between the iSRR layer, spherical steel plate, and the bottom FRP flange.

In the standard scenario the maximum resistance of the SP20 is computed to be 495kN. The failure of the specimen occurs in two stages. First cohesive damage and subsequent separation at the iSRR interface layer diminishes shear interaction with the spherical steel plate and the FRP flange, resulting in a lower stiffness of the connection. This is initiated around a load of 100kN, and progresses to a maximum at a load of 366kN. The second part of the failure mode is delamination in the bottom flange, creating a crack after which the resistance is lost. Delamination is initiated around a load of 366kN, and reaches a maximum at 495kN.

The models of SP20 with a 2° angular deviation or a positional displacement all the way off-centered result in a reduction of resistance to respectively 434kN and 406kN. Asymmetric failure modes are observed due to different lengths of the leverarm created by the spherical steel plate. Due to different amounts of bending of the steel plate at either side of the bolt, the FRP flange is forced to bend more on one side than the other. The result is different moments of delamination for either side of the connection.

6 Experimental Campaign

This chapter covers the experimental campaign, where the design SP20 is produced and tested. The test series consists of two static tests (S1/2) and two cyclic tests (C1/2). First the production process of the specimens will be explained, after which two separate sections are dedicated to the static and the cyclic tests. The sections include the test set-up, results, failure modes, and preload loss analyses. The static tests will also be compared to the numerical results and for the cyclic test an extra subsection is dedicated to describing a fitting F-N curve.

6.1. Production of the Specimens

The FRP decks are delivered by FibreCore as sandwich decks with two connector holes drilled in the FRP facing. The cavity in the foam to place the steelshot and resin is already cut out beforehand. The production that is left to do is filling the hole with the combination of steel-shot and resin, and placing the steel package. The spherical coverplate is externally produced with a CNC machine according to the dimensions in Appendix B. The following steps are taken in the assembly process:

1. Placing an injection straw in the hole. This straw reaches the bottom of the hole (the decks are upside down), and will facilitate the resin to be poured all the way to the bottom of the block.
2. Pouring steel shot in the hole in the deck, around the injection straw (see Figure 6.1a). The steel shot is densified by vibration. After densifying the steel shot more steel shot is added until the top of the steel shot is level with the middle height of the FRP bottom flange.
3. The resin is injected with a caulk gun through the straw from step 1, this way it is made sure that the resin reaches all the way to the bottom of the steel shot. During this step the straw is gradually lifted upwards while injecting, until the straw is eventually fully out of the mixture. The idea behind this method is that the level where the resin is injected keeps rising up by lifting the straw up. If all is done well, this method should ensure a well mixed mixture of resin and steel shot. Lifting the straw also ensure that the resin has less chance to collect at the bottom and push out all the steel shot.
4. The steel package is pushed as a whole into the resin/steelshot-mixture, until the spherical coverplate is in contact with the reinforced resin coming out of the FRP deck. As the steel package is pushed inside, resin/steelshot will overflow out of the hole, creating a layer of resin/steelshot between the FRP and the spherical steel plate. The aim is to create a resin/steelshot interface between the FRP and the spherical steel plate of about 3mm (see Figure 6.1b).

The production of the specimens was done on two different occasions. First specimens C1 and C2 were produced at the same moment, a few days later specimens S1 and S2 were produced, also at the same time. During the production of C1 and C2 it was found that pure manual compression was not sufficient to push the steel package all the way into the deck. Specimens C1/C2 were wiggled back and forth a lot (excessively) to try and get them deeper in the deck, which eventually worked. A result however could be that gaps opened up around the bolt head during this excessive movement, and that air traps or less well mixed areas occur.

(a) The steel shot is placed around the straw **(b)** Result of the production phase

Figure 6.1: Overview of the production

To overcome the problem of wiggling too much, specimens S1 and S2 were lightly hammered on the top of the bolt rod to mimic vibration of the deck. A boltnut was screwed to the top and was hit, as to not damage the USB strain-gauges. Although this worked better than just pressing from above, it was still needed to lightly wiggle the steel package back and forth. This way of producing was however still a lot easier, and ensures that the resin/steelshot really embraces the steel package as much as possible.

6.2. Static Tests

The static tests are aimed at finding the ultimate load possible before breaking of the connector or the bridge deck itself. The machine that is used can load the specimen in compression up until 600kN, which should be enough to break the specimen according to the numerical analysis. The machine itself only measures the loading and global displacement applied. In addition Digital Image Correlation (DIC) will be used on one side of the specimen.

6.2.1. Test Set-Up

Figure 6.2a and Figure 6.2b display a scheme and a photo respectively of the placement of the test specimen in the machine. Note that the left connector (S1) is the one being tested, the right connector (S2) merely hangs out of the machine since it was not possible to cut the FRP deck into two pieces before the tests were going to be carried out. To perform test S2 the block would be dismounted and shifted to the left, such that S2 would be tested and S1 is hanging out of the machine. The following steps are taken as to prepare the specimen for the test, after injection of the specimen:

1. With the block upside down, the following parts are placed in order on the spherical coverplate: steel baseplate, normal coverplate 100x100x20, conical washer, nut.
2. Preloading the bolt to around 280kN, letting the bolt relax for 40-60 minutes, and reloading again to 280kN. The preload force in the bolt is measured with strain gauges embedded 50mm into the bolt, the data being collected through a USB-cap attached to the end of the bolt.
3. The deck, with steel baseplate attached and the bolt preloaded, is placed into the machine.
4. Applying the DIC paint on one side of the deck. DIC paint is applied after placement in the machine to prevent damages to the paint during placement.
5. Placing the cork pad exactly on the top of the deck, centered above the tested connector.

The machine applies load from the bottom steel block, the top block remains still in place all the while. The machine itself measures the global displacement, which results can be influenced by the stiffness of the machine. DIC will be used to both be able to track the pure vertical displacement, as well as capturing strains and stresses on the outer surface of the deck.

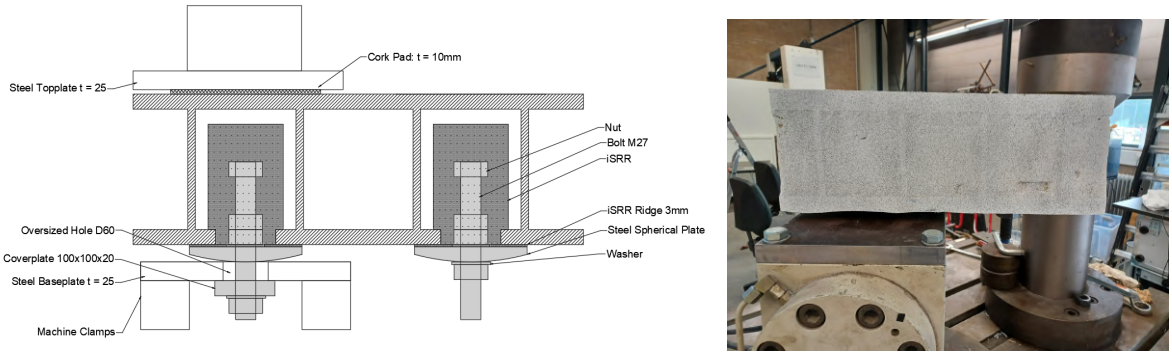

(a) Scheme of the test set-up

(b) Placement in the machine with DIC paint applied

Figure 6.2: Static test set-up

A white base-layer of paint is applied to the block, onto which small black dots are sprayed with a paint-gun. These dots are tracked by the DIC-system in 3D, and hence the strains in the deck can be obtained. Extra stickers are applied to the top and bottom steel plates attached to the machine. By tracking the distance between these stickers, the purely vertical deformation of the block and corkpad can be measured (hence being a virtual local LVDT). The DIC-system has a capacity for approximately 1000 measurements of the deck per test. To be on the safe side a measurement period of 3s was chosen. In the end for test S1 and S2 respectively 411 and 308 measurements were taken.

The machine stroke initially was set for test S1 to 0.01mm/s (see Figure 6.3). As no damage was expected to occur in the early stages and to limit the testing time, the machine stroke increased to 0.04mm/s. After the first cracking sounds the stroke was lowered to 0.02mm/s at 120kN, to decrease the machine stroke again to the original 0.01mm/s at 220kN. Test S2 directly started with a stroke of 0.04mm/s and decreased to 0.02mm/s at 90kN. The final machine stroke of was set to 0.01mm/s at a load of 210kN.

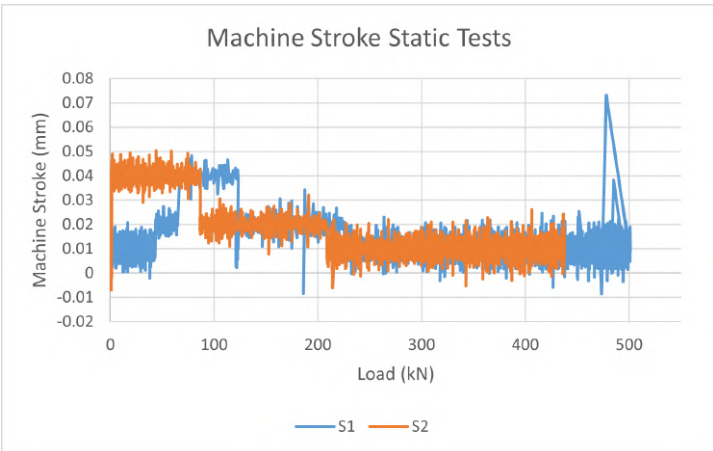

Figure 6.3: Machine stroke of the static tests

6.2.2. Results and Failure Modes

The load-displacement graphs of tests S1 and S2 are plotted in Figure 6.4. Both subfigures contain per test the load-displacement graph as measured by the machine itself (the machine stroke), and the pure vertical displacement measured by the DIC. For test S1 a near perfect match is seen, for test S2 a mismatch occurs. During the first stage in test S2, until approximately 6mm of total deformation, both the DIC and machine stroke measurements match almost perfectly. After that point the machine starts measuring a larger displacement than the DIC for the same load level. An explanation is that the FRP deck is rotating a slight bit due to not being perfectly horizontal mounted or produced. As such, the total machine stroke consists of both a horizontal and vertical displacement, where the DIC measures

purely the vertical deformation. The two measurements start to match each other again at the return stage of the test, as the rotation is undone and the horizontal component of the deflection becomes insignificant.

The ultimate resistances of tests S1 and S2 are respectively 501kN and 438kN. The propagation of the test went for both cases quite similarly, even though the final resistance of S2 is 12.5% lower than that of test S1. Appendix C displays the DIC figures of both tests at three significant moments. The figures are referred to as S2.1 for the first significant moment of test S2.

Generally around a load level of 60kN the first cracks were heard. These cracks were relatively loud, but shallow in sound, and are attributed to cracking of the foam core. Around 120kN the first smaller and more faint cracks were heard, and occurred in the FRP itself. Around 370kN of loading major cracks occurred in the foamcore at the outside of the block (S1.1/S2.1). Due to large deflections the foam is squeezed out and cracks due to low tension resistance. At the same time strains are starting to occur in the top of the bottom flange, accompanied by sounds attributed to the onset of delamination in the FRP. More strains occur until cracks start appearing in the bottom flange around 430kN to 450kN of loading (S1.2/S2.2). For test S2 the final failure occurred right after at 438kN, where the crack in the bottom flange suddenly extended into the web (S2.3). Test S1 continued to build more resistance, and got its first failure at 500kN due to an extra crack in the bottom FRP flange. The load dropped to 495kN, and built up to 500kN again. Failure occurred at 501kN, dropping the force to 476kN after which the test was stopped (S1.3). The same ultimate failure mode as test S2 was observed, where the crack in the bottom flange extended into the web of the FRP.

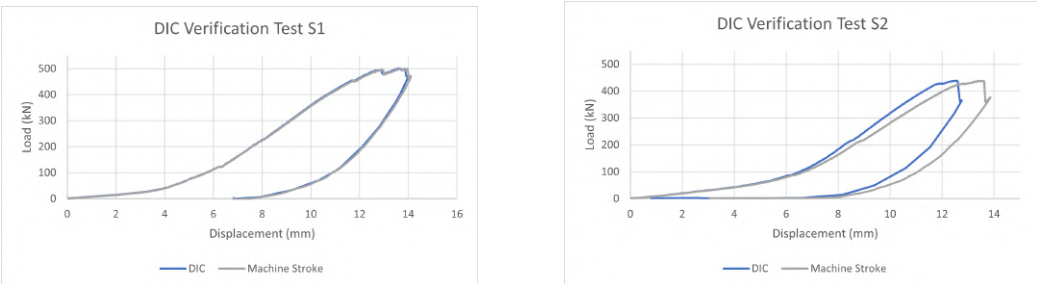

(a) S1 **(b)** S2

Figure 6.4: DIC vs. Measured machine stroke displacements

6.2.3. Preload Loss

The specimens are preloaded as described in the former section. Both specimens underwent two cycles of preloading, the before (1) and post-relaxing (2) loading. Table 6.1 displays the steps of the applied torgue to reach a preloading level of approximately 270kN - 280kN. It is seen that specimen S2 already reached the required preload level at 900Nm torgue, where specimen S1 reached that level at 1200Nm of torgue. No clear explanation as to where this difference originates from is found.

Table 6.1: Torgue required for preloading S1 and S2

Torgue (Nm)	Cycle	S1	S2
480	1	102	150
900	1	185	283
1200	1	265	-
1230	2	271	-
870	2	-	288

Figure 6.5 displays the diagram of preload-force plotted against the applied load during the static test for tests S1 and S2. With different shades the loading stage and the unloading/post-failure stage of the tests are indicated.

Test S1 has an initial preloading force of 258kN. The preload force reduces consistently until failure, except that at a load of 86kN a sudden increase in the slope is observed of the preload force. The preload force reaches its absolute minimum of the loading stage at a load of 412kN. The preload

force at that moment being 189kN means that the maximum preload loss during the loading stage amounts to 26.7%. At failure the preload force starts increasing, from 189kN to 200kN. At last, during the unloading stage, the preload force decreases again until a final preload force of 174kN. The total preloadloss therefore totals to 84kN (32.6%) over the entire duration of the test.

Test S2 started with a preloading force of 282kN, and dropped in its loading stage to a minimum of 255kN, being a loss of 11.5%. This minimum in preloading force occurs at a load of 324kN. After this moment the preloading force increases again until 261kN at which point the ultimate resistance was reached. During the unloading stage an extra loss of 11.1% from 261kN to 232kN occurs. The total loss of preload force over the total duration of the test, loading and unloading, amounts to 17.7% from 282kN to 232kN.

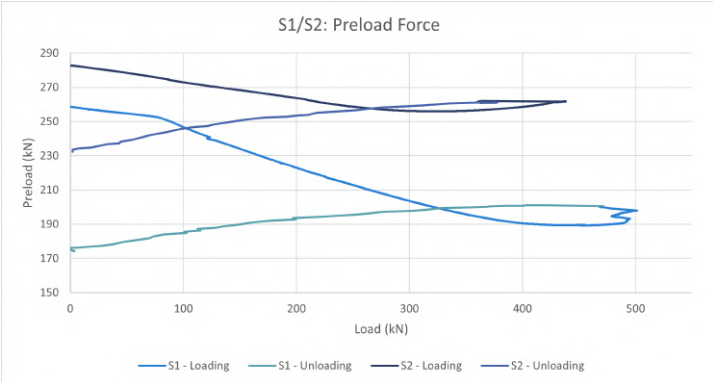

Figure 6.5: Preload-load diagram S1/S2

It is seen that test S2 has a lower loss of preload in both absolute values (50kN vs. 84kN) as well as in percentage (17.7% vs. 32.6%), while also have a higher initial preload force. The differences between these two tests might originate from that the same coverplate and conical washer were used for both tests.

6.2.4. Comparison Numerical and Experimental Results

The DIC and machine stroke measurements as presented in Section 6.2.2 include the deformation of the corkpad used in the experiments. The numerical analysis does not make use of a corkpad, therefore it is of importance to use the DIC to obtain vertical displacements excluding the deformation of the corkpad. Three measurements are taken between the bottom steelplate and the three locations:

1. Above each web, vertically in the middle of the top flange.
2. Horizontally between the webs, vertically in the middle of the top flange.

Figure 6.6 showcases the load-displacement graphs for the two static tests, where the displacement is measured between the bottom steel flange and the significant points in the top flange.

For both tests it is seen that the displacements are the highest for the right side of the block, and decrease as measurements are taken in the middle or above the left web. These measurements stem with the observation during the static tests that the block tended to rotate clockwise. This behaviour is a result from an imperfect alignment of the top of the deck and the machine head pressing on the deck. Attempts were made to create a perfectly straight interface, but this would result in a more off-centered placement of the bolt in the bolthole. The latter was more important for these tests. The result is that the distribution of force on the top flange was not entirely uniform.

Figure 6.7 compares the numerical results to the deformations as measured by the DIC, excluding the corkpad deformation. It can immediately be observed that the stiffness of the two static tests match almost identically for the first part of the test, but the numerical model has a lower stiffness. Regardless of this difference in stiffness, S1 and the numerical results match almost perfectly in ultimate resistance. Especially when compared with test S1, it is seen that around same load levels the same type of behaviour occurs. Both S1 and the numerical results reach a load level of 495kN, after which a small drop in load occurs. After reaching back once more to 500kN exactly, both S1 and the numerical analysis experience their actual failure.

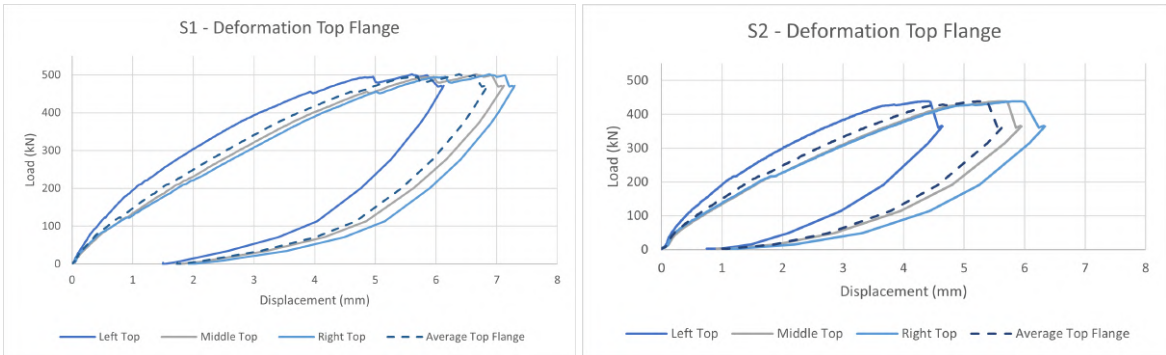

(a) S1 **(b)** S2

Figure 6.6: Top flange deformations

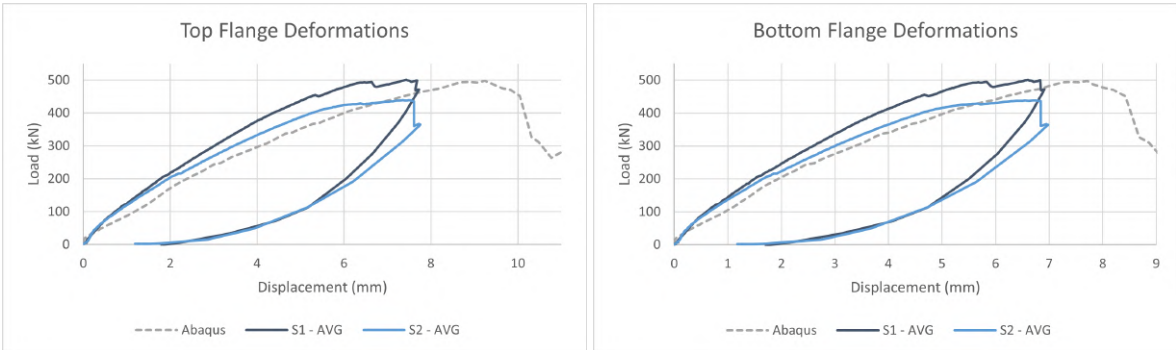

(a) Top Flange **(b)** Bottom Flange

Figure 6.7: Load-displacement graphs comparing experimental and numerical results

Test S2 does not match the ultimate resistance of approximately 500kN. Different factors could be of influence, from production mistakes to small differences in handling of the block. However, the most notable difference between tests S1 and S2 is that both tests are performed on the same block, only on other sides of that block. Hence side S2 could be impaired due to the prior testing of S1, for example by small cracks that propagated into the side of S2 during testing of S1.

The failure mechanism of the experiments and numerical analysis are quite similar. Delamination is primarily observed in the early stages in the upper part of the bottom flange of the FRP. During the experiments cracking occurs in the flange, which afterwards propagates into the webs leading to final failure. The FE-model shows similarly that delamination forms into a crack, but the propagation is not shown to be into the web. This is due to that the Z-shape that the blocks are produced with is not entirely well modelled. Purely a tie constraint is added between the webs and the bottom flange of the FRP, which could be improved if need be in later models. However, the increased computational time might not outweigh the benefits as the model represents the ultimate resistance and failure mode quite well already.

The difference in stiffness mentioned earlier is the largest error between the experiments and the numerical analysis. Figure 6.2 displays the lines drawn to approximate the stiffness of the three measurement series. Table 6.8 shows the stiffness of each test numerically in kN/mm. Test S1 has the highest stiffness with 95.2kN/mm. The FEA results show a stiffness of 75.1kN/mm, which is 21.1% lower than for S1. Test S2 has an approximate stiffness of 86.2kN/mm, such that the stiffness from FEA is 12.9% lower.

Figure 6.7a displays the load-displacement graph where the displacements are measured at the top flange as described earlier this section. Figure 6.7b displays the deflections as measured at the bottom flange of the FRP. As cracks form in this part of the model, it is best to take measurements below the point where the cracks occur. This results in that the measurements are taken in the bottom flange at the same horizontal locations as before (in the middle and under both webs), where vertically they are taken at the lowest point in the bottom FRP flange.

Table 6.2: Stiffness in kN/mm

Test	Stiffness (kN/mm)
S1	95.2
S2	86.2
FEA	75.1

Figure 6.8: Stiffness comparison of S1, S2, and FEA

Table 6.3 compares the displacements at the maximum load level of S1 and the numerical analysis at the top and the bottom FRP flange. S2 is left out of the comparison as the ultimate resistance does not match with the two others, which is likely due to the prior test on S1. The table shows that the maximum displacement of the numerical analysis is 24.4% more than S1 in the top flange, compared to 16.6% for the bottom flange. The difference between these measurements is that the deformation of the top flange and the webs is not included in the bottom flange measurements. As the difference in displacement is the smallest when measured at the bottom flange, it can indicate that for example the foam-core or the webs have a too low stiffness in the Abaqus-model.

Location of Measurement	S1	Numerical Results	Increment
Bottom Flange	6.61	7.71	+16.6%
Top Flange	7.42	9.23	+24.4%

Table 6.3: Displacements at various locations (in mm)

6.3. Cyclic Tests

The cyclic tests are performed after the static tests and are used to assess the fatigue behaviour of the connection. Since only two tests will be conducted, the primary goal of the cyclic test campaign is to assess the behaviour and resistance of the deck under cyclic loading that is realistic to occur in real world applications, for which Section 3.3.2 indicates that a load range of 85kN is expected in FLM4. As not all decks will have the exact same geometry and hence have different load distributions, the load level is chosen to be 90kN initially, as that is the most expected load per wheel being half the axle load.

The target amount of total cycles associated with 90kN is determined to be 500.000 cycles, with a range of 9kN - 90kN (R = 0.1). The deduction for the estimated total of 500.000 cycles can be found in Appendix D.

6.3.1. Test Set-Up

The same machine is used for the cyclic tests as for the static tests. No DIC is applied, since DIC is not able to capture the 4Hz frequency of the cyclic test. The local measurements are this time taken with four LVDT's, placed around the block on the bottom facing of the FRP at the location of the webs. At these locations on the FRP bottom facing steel L-plates are glued. The FRP at the location of the

L-plates is cleaned lightly with aceton, after which the plates are glued to the FRP with 2-component glue. The base of the LVDT's is attached to bottom moving part of the machine (pushing up in the test) by use of magnetic holders, the tip of the LVDT's rest on the steel L-plates. The result is that the LVDT's are measuring the relative displacement between the FRP bottom facing and the steel baseplate, hence capturing the bending of the FRP. Extra care is therefore put in placing the L-plates straight, such that only vertical displacement is measured and no sideways slip of the LVDTs is taken into the measurements. Figure 6.9a shows the sideview in the machine, where the base of the LVDTs is clamped to the machine/baseplate. Figure 6.9b depicts the way the tip of the LVDT is placed on the L-profile.

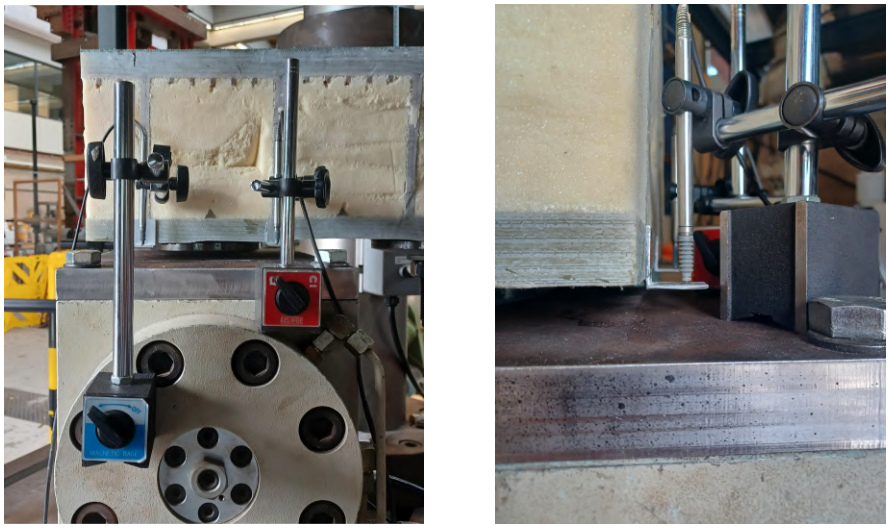

(a) LVDTs placed on steel baseplate **(b)** LVDT tip on L-profile

Figure 6.9: LVDT placement for the cyclic tests

Similar to the static tests, the specimen contains two connectors to test. Figure 6.10 displays the placement of LVDTs during both tests. In between the tests the block was shifted sideways to mount the new connector. At last the cork pad is placed exactly central above the two webs of the tested connector.

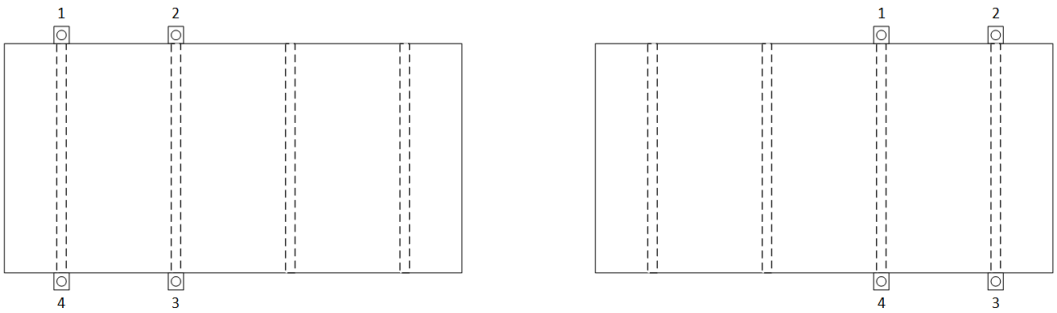

(a) Test C1 **(b)** Test C2

Figure 6.10: Schematic top view of LVDT placement for the cyclic tests

6.3.2. Results

Two tests are conducted, test C1 and test C2. The results of the full duration of the tests can be found in Figure 6.11. The main testing goal was to surpass the 500.000 cycles with a load range of 9kN - 90kN. As the first test was going on during the weekend, the test was extended until 1.338.080 cycles. No significant damage occurred yet at this point, the graphs show that the average and the range of the displacement remained constant. Due to initial time limitations it was decided to double the load

range to 18kN - 180kN. A total of 33.940 cycles were reached at this elevated load level when breaking of the webs occurred.

Test C2 had as main goal to be a long-term test. The starting load range of 9kN - 90kN was ran until about 2.084.640 cycles, but no significant change in the average and range of displacement occurred. The load level was increased 1.5 times to 13.5kN - 135kN to create more data points for an indication of an F-N curve. An additional total of 394.960 extra cycles were recorded at the elevated load level before a similar failure mode occurred as during test C1.

Figure 6.11a displays the average displacement per cycle for both tests C1 and C2 combined. The following points are of attention:

1. Test C1: At 1.3 million cycles the increase in displacement is seen, which relates to the elevated load range. At this point there is a small peak down, to about 1.8mm. This peak comes from opening the machine to recalibrate the input parameters to achieve the new desired load level.
2. Test C1: The final peak at 1.33 million cycles is the breaking point of the webs. The machine was set to stop measuring after 8mm of displacement, but is cut off in this graph.
3. Test C2: The test was stopped for about half an hour after finishing the load range 9kN - 90kN (after 2.1 million cycles). During the first stage it was observed that the block was mounted with an angular deviation, causing the block to exert more pressure on the side of the block of LVDTs 3 and 4. In between the stages an extra cork pad was added with a counter angle to the block, such that the load distribution was uniform again. The negative peak in displacement relates to opening the machine.
4. Test C2: The average machine displacement is lower in the second stage of C2. The addition of the extra cork pad makes that the machine lowers less per stroke, such that a drop in the absolute average displacement is observed. Figure 6.12b displays the LVDT measurements of the local relative displacement of the bottom web, where the influence of the corkpad is logically not observed.

Figure 6.11b displays the range of the displacement each cycle. This graph therefore does not contain information regarding the total displacement, but it does tell something regarding the stiffness of the specimen after many cycles. A horizontal line would indicate no decay at all, an increasing line would indicate damage and subsequent failure. For both tests it holds that at the start of each new loadcycle the displacement range reduces to a stable level. This is expected behaviour, but the amount of the reduction can be slightly magnified by the applied corkpad on the top of the block.

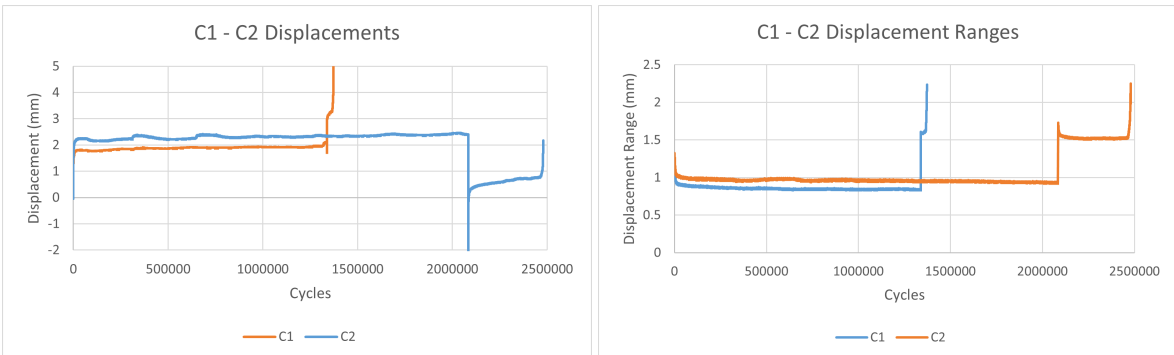

(a) Absolute average displacement

(b) Range of displacement per cycle

Figure 6.11: Displacement graphs or the full duration of cyclic tests C1 and C2

Figure 6.12 shows the range of the displacement per cycle measured at the LVDTs. A positive displacement is defined as extension of the LVDT, hence measures the relative downward bending of the bottom flange of the FRP block. Both the graphs of C1 and C2 show that two LVDT's experience a high displacement range, and two LVDT's experience a range almost equal to zero. This behaviour comes forth from rotations of the block each cycle. As the block is not perfectly straightened out, the pressure on one side of the block is higher than on the other side. The block hence rotates until the pressure is equal again. If only rotation occurred, it would mean that the two sets of LVDT's measure

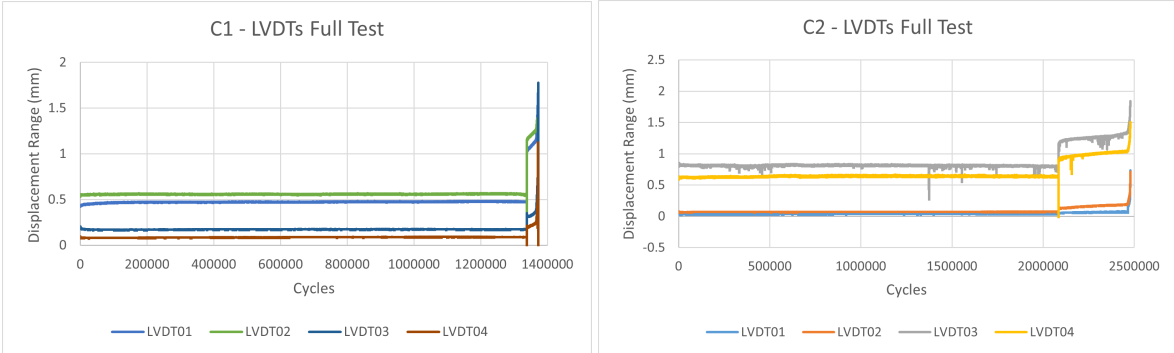

(a) C1 **(b)** C2

Figure 6.12: Displacement graph of LVDTs for the full duration of the tests

displacements equal in magnitude but opposite in direction. It can be seen that this is not the case here, as all displacement ranges are above zero. Hence the displacements are a superposition of rotation of the block and standard vertical motion.

Furthermore it is seen that the LVDTs stabilize in the range of 9kN-90kN to an almost flat curve, where after increasing the load a continuous increasing displacement is seen. LVDT 03 shows spikes in its behaviour, this is due to the LVDT itself sometimes malfunctioning by getting stuck. Zooming in into the parts of the graph with increased load ranges yields Figures 6.13a and 6.13b. In both figures the moment that the first crack occurs can well be seen by the sudden increase in displacement ranges. This start of the crack propagation occurs for test C1 after 29.060 cycles (85.7%) and for test C2 after 376.130 cycles (95.2%). In both tests almost all LVDTs, as expected, experience increasing displacement ranges the closer the specimens gets to failure. Only LVDT 02 in test C1 experienced close to failure a reduction of displacement range, this occurred as the steel L-plate the LVDT was attached to fell of the specimen during the test.

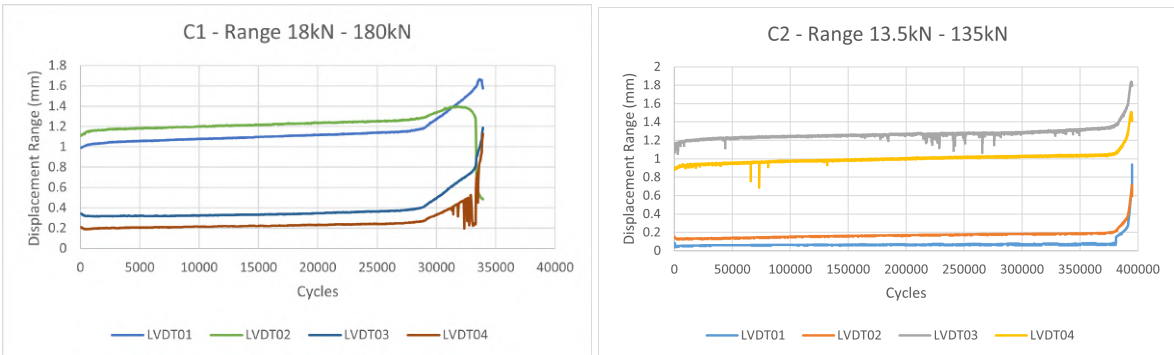

(a) C1 **(b)** C2

Figure 6.13: Displacement ranges of LVDT's for the high load ranges

6.3.3. Failure Modes

The displacement graphs show a relatively sudden failure of the specimen, in just a couple of cycles ($\approx 4-6$) a full failure is reached. This indicates a governing failure mode, rather than various failure modes occurring after each other. Test C1 failed without supervision, the failing of test C2 was supervised. Test C2 started to show increasing deformation, which grew exponentially. A crack was seen in the bottom flange, which started in the middle of the flange and grew towards the webs. Once the crack reached one of the webs a quick failure occurred in a single cycle of that web on that respective side of the block. In the following 3 cycles all sides of the webs cracked and the test was stopped automatically. The rotation of the block contributes to that the webs did not crack in one full go, but that each web cracked through in two stages.

The web cracks are displayed in Figure 6.14. The first failing web cracked due to cyclic delamination

and subsequent buckling, the remaining webs broke as a result of buckling due to a sudden increase of the load on the webs. Figure 6.14c shows a sketch including the trajectory of the crack leading to failure. The following stages are indicated:

1. Initiation of the crack in the bottom facing due to delamination. This crack was visibly opening up and closing during the test. After full unloading this crack was almost not visible anymore.
2. Propagation of the crack towards a web. The crack propagates diagonally through the fibre mats, creating reaching further and further each cycle.
3. First full fracture of the web. As the crack reaches the web the web is overloaded and fractures due to loss of strength and buckling resistance.
4. As one web failed due to buckling, the other webs are failing due to overloading as all loads are transferred through that web only.

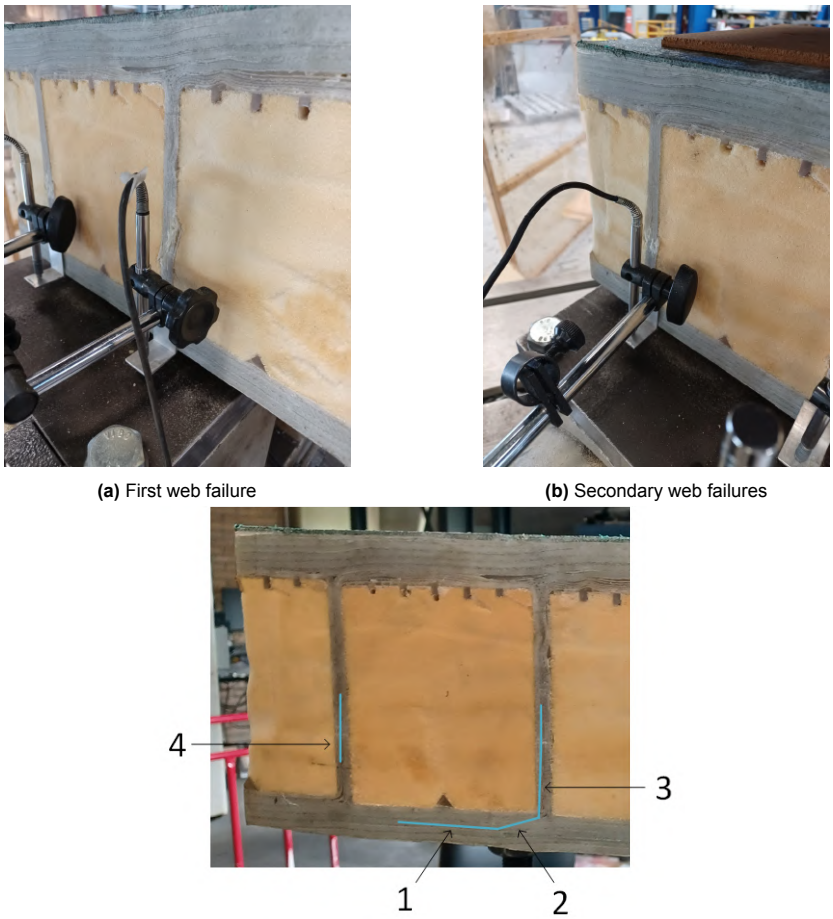

(a) First web failure

(b) Secondary web failures

(c) Cyclic test failure progression

Figure 6.14: Web failures of cyclic test 2

6.3.4. Preload Loss

The goal for the initial preload level was to reach a preload force of 270kN, equal to the loading as in the static tests. For the preloading of the static tests 900Nm and 1200Nm of torque was needed to reach approximately 270kN of preloading force. For the cyclic tests the full capacity of the torgue gun (1350Nm) was used, resulting in a preload force of 269kN and 246kN for test C1 and C2 respectively. No clear explanation is found as to why this difference exists between the preloading of the static tests and the cyclic tests.

During the cyclic tests the preload force has been measured continuously. Figure 6.15 plots the preload force against the total endured cycles in the same graph as the range of the displacement. The preload force reduces in both tests gradually, even when the displacement range stays the same. This decrease happens in two different patterns for the two tests. Test C1 follows an almost parabolic like shape. After a quick preload loss at the start due to initial loading the rate of preload loss becomes less the longer the test continues. Test C2 also experiences the surge in preload loss at the start of the test and follows with two linear stages rather than parabolic like behaviour. The first linear preload loss pattern is steeper than the second and lasts until about 700.000 cycles. Even though the pattern of the preload loss and the initial preload levels are different from each other the total loss during the low load level stage is similar. C1 and C2 respectively experience a 8.6% and a 7.7% loss of preload during this stage. These results however do not take into account that test C2 ran for 43% longer than test C1. If test C2 is measured after 1.4 million cycles (full duration of C1), a relative loss of 6.5% is measured.

After the low load range stage, both the tests are subjected to their respective higher load range. The sudden load range increase induces a sudden decrease in preload force. This is in accordance with the static tests, where the preload force also reduces with a higher applied load. The extra preload loss is however small in the total aspect of the test, as is shown in Table 6.4. The total preload loss ranges between 9.3% and 11.1%, measured from the initial preload force until the preload force right before failure occurred.

Table 6.4: Preload force and losses at significant moments in the cyclic tests

	C1	**C2**
Initial Preload Force (kN)	268	247
Preload Force Before Load Increase (kN)	245	228
Preload Force Before Failure (kN)	238	224
Preload Loss 9-90kN load range (%)	8.6	7.7
Preload Loss Elevated load range (%)	2.9	1.7
Total Preload Loss (%)	11.1	9.3

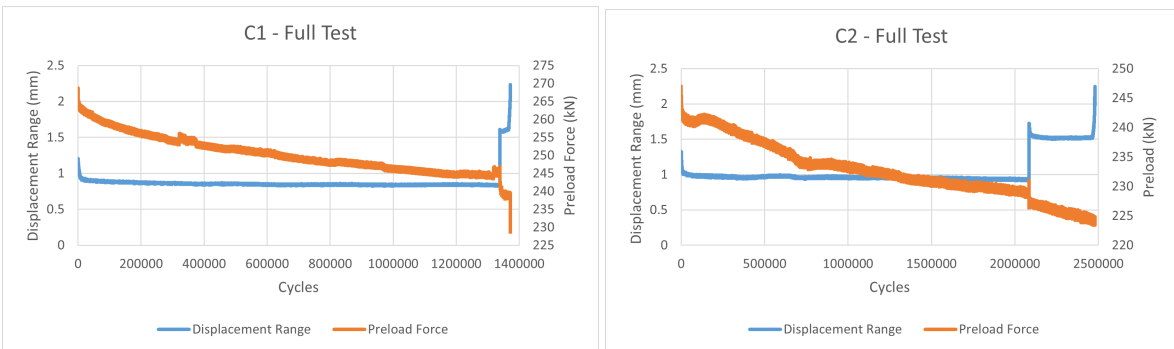

(a) C1 **(b)** C2

Figure 6.15: Preload and displacements graphs of the cyclic tests

6.3.5. F-N Curve

The results from the static tests and the cyclic tests are plotted as an F-N curve. This F-N curve displays similar failure modes for both the static and the cyclic test. The static test failed by means of delamination in the bottom facing, which carried through into the webs. The cyclic test failed by a small crack propagating into the webs as the test duration increased. A point of difference in behaviour is found in the behaviour of the spherical steelplate. During the static tests the plate yielded, during the cyclic tests this was not the case. However, this only resulted for the static test in a loss of stiffness, and did not seem to contribute to the failure of the specimen.

From this point it is concluded that for the design of the steelplate with thickness 20mm the failure mode will remain contained in the FRP. As such, the F-N curves presented in Figure 6.16 are purely

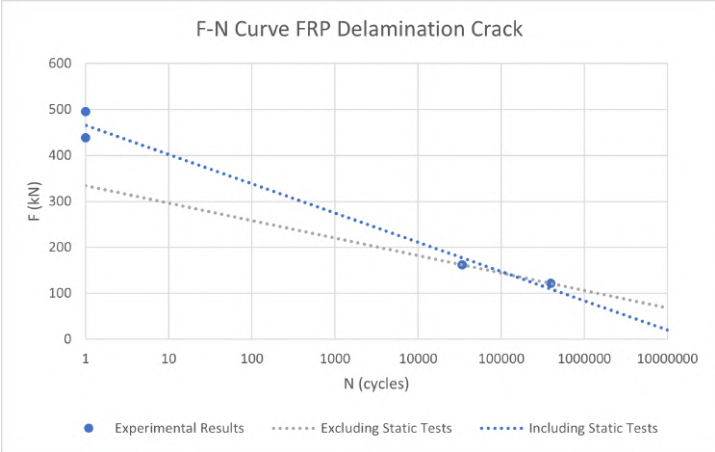

Figure 6.16: F-N curve FRP delamination failure

FRP related F-N curves. Note that the data points from the cyclic tests are only covering the higher load ranges, and do not include data from the range 9kN - 90kN. Two curves are plotted, one including the static tests and one including only the cyclic tests. If the static tests are included, a curve with m = 8.5 is found. Whenever only the cyclic tests are included, a curve with slope m = 13.6 is found.

The tests initially started with the goal to find the resistance against the load range 9kN - 90kN (Δ= 81kN). Extrapolating the data from the tests can be done as said with and without the static tests. Excluding the static tests yields expected failure for the range 9kN - 90kN at 4.6 million cycles, including them gives a resistance of 1.1 million cycles. However, both tests C1 and C2 exceeded 1.1 million cycles at this load range, indicating that the F-N curve including static test results is conservative. Two reasons can be the case for the conservative nature of the curve. First and foremost is the importance to recognize that tests C1 and C2 are plotted in the graph as if the specimens were only subject to the higher load range. In reality these load ranges were subsequent to 1.3 million and 2.1 million cycles already at the 9kN - 90kN range. Testing on a new and unaffected specimen will likely increase the resistance of the specimens under higher load levels. Secondly it could mean that failure modes are not exactly representative in the same curve. After all, the steel spherical plate bent a lot during the static tests, where it did not during the cyclic tests. However, it for sure can be said that the curve with m = 8.5 is conservative as the projected failure level is surpassed by the tests.

6.4. Conclusions

This section covered the experimental campaign, including set-up and results of the static and cyclic tests. Moreover, the static test results were compared with the numerical results and an F-N curve is presented based on the cyclic test results.

The static tests S1 and S2 respectively have an ultimate resistance of 501kN and 438kN, similar to the numerical analysis yielding a resistance of 498kN. Even though the resistance is similar, the stiffness of the FEA is 21.1% lower than that of test S1 and 12.9% lower than S2. Regarding preload force S1 performed worse than S2, with respective losses of preload force of 32.6% and 17.7%. The numerical analysis follows initially similar behaviour as the experiments, but afterwards fails at the iSRR ring at which point the clamping package gets disrupted.

The cyclic tests C1 and C2 sustained respectively 1.3 million and 2.1 million cycles at 4Hz at a load range 9kN - 90kN. No damage occurred and the displacement remained constant after 2.1 million cycles at maximum, such that the load ranges were increased. Test C1 failed after an additional 33.940 cycles at a load range of 18kN - 180kN, test C2 failed after 394.960 cycles at a load range of 13.5kN - 135kN. The failure of both specimens was initiated by a horizontal crack opening up in the bottom flange of the FRP. The crack propagated towards one web, after reaching that web the other web failed due to buckling. As the failure occurs in the FRP similarly to the static tests the F-N curve can include the static results. An F-N curve with slope m = 8.5 at a base of 1 cycle at 465.32kN is found.

7 Recommendations

To enhance the level of detail and completeness in the research towards the iSRR connector subjected to wheel-loading, the following points are advised to be improved or researched:

- Due to limited time and testing capability, a decision on the plate to order had to be made early in the research. The SP20 was ordered for production, but the results show that this type of plate has a very high resistance and a fatigue life longer than expected to be necessary. Future research could investigate the option for the SP15 plate more deeply, as the ultimate resistance of this plate also exceeded the requirements. Using the SP15 plate can save a lot of steel if measured per bridge.
- The case-study regarding the bridge Nieuw-Vossemeer results in the load levels that were designed for. However the geometry of this specific bridge might yield different results than if a set of bridges was studied. Including extra detail to the models will give a complete view of the expected load levels rather than an indication. Possibilities for a more detailed FE-model include: including stiffness parameters for the hybrid interaction at the connections and modelling of the stiffness of the steel superstructure.
- As no option was available to cut the FRP decks, two connectors were embedded in one bridge deck. By testing the second connector after failure occurred in the first connector, the resistance might be affected. It can be seen that the ultimate resistance of S2 is significantly lower than S1. It is recommended to split the block such that only one connector is embedded in each test specimen.
- This thesis did not aim at determining the optimal material properties for the numerical modelling, as such some discrepancies can be observed between the behaviour of the FE-models and the static tests. The ultimate resistance and failure mode of the FE-model matche very well with the experiments, the stiffness is however off by up to 25%. More detailed research into the interactions between the FRP, the reinforced resin, the foam core, and the steel plate could bring useful insights and improve the stiffness approximation.
- The F-N curve is based on two cyclic tests, which both had a prior loading of one to two million cycles at 9kN-90kN. With more time on hands it would benefit the accuracy to perform separate 9kN-90kN tests to failure, and do the elevated load level tests on virgin specimens.
- The connector as proposed is subject to some limitations and can benefit from design improvements. As the connector was rotated 2°, the bottom coverplate did not have full contact anymore with the steel girder. This mostly results in a reduced preloading package and bending in the ordinary coverplate due to preloading. Rotation adjusting nuts could benefit this cause. Furthermore the off-centered placement results in a cavity opening up for water to seep into the oversized hole. To reduce water accumulation two solutions can be adapted. Either small holes are drilled in the coverplate to let water drip out, or the area around the spherical coverplate can be sealed off with a squeezable foam ring, preventing water from entering.

8 Conclusions

The use of modular FRP bridge panels in infrastructure can greatly help the surge to a more sustainable construction sector. The main limitation of these panels is currently the lack of a predictable and demountable shear connector. Therefore, the primary objective of this thesis was to develop an iSRR connector capable of enduring the anticipated local wheel load levels and geometric deviations occurring in bridge applications. The main innovative design feature is the spherical steel plate between the FRP deck and the steel girder flange. By making this design spherical the plate allows for relative rotations between the flange and the deck. Making this plate with a diameter of at least 150mm enables it to function as a coverplate spanning the oversized hole in the girder, and limits bending of the FRP bottom flange.

To find the expected load levels occurring in bridge applications, a FE-model is made of a case-study bridge in the Netherlands. The following list of requirements regarding load levels and geometrical tolerances is found that are applicable to this connection:

1. ULS: Load Model 2 of the Eurocode is governing, with a localized wheel load of 188kN on a tire area of 400mm x 400mm.
2. FLS: Fatigue Load Model 4b is governing with a maximum axle weight of 180kN. Due to the size of the wheel the load dissipates to multiple connectors, leaving a maximum wheel load of 85kN. This will be exerted around 500.000 times in a time span of 50 years.
3. Oversized holes with a diameter of up to 60mm in the girder flange are needed to account for positional tolerances.
4. Since the bolts will be preloaded and oversized holes are used, coverplates on both sides of the girder flange are needed.
5. Tilting of the girder flange and production tolerances lead to a maximum angular deviation between the bridge deck and the girder flange of 2°.

The final design is presented in the report, and subjected to numerical analyses and experimental tests. The following results are found:

1. The experimental ultimate resistance is measured to be up to 501kN, this being 0.6% more than the numerical analysis at 498kN.
2. The fatigue resistance of the connector is at the load range 9kN - 90kN at least 1.3 million cycles, and can reach 2.1 million cycles without damage. Increased load ranges of 13.5kN - 135kN and 18kN - 180kN were sustained for respectively 394.960 and 33.940 cycles until failure occurred.
3. Positional tolerances influence the ultimate resistance of the connector. FE-models show that a 2° rotation yields an ultimate resistance of 434kN. Furthermore a straight connector placed fully off-centered has a limited resistance of 406kN.
4. The stiffness of the tested connection reaches up to 95.2kN/mm. The FE-model underestimated the stiffness with 21.1% to be 75.1kN/mm.
5. Both the static and cyclic tests experience initial failure by delamination in the bottom facing of the FRP, continuing into failure of the webs by propagated cracks.

References

Abaqus. (n.d.). *Abaqus Analysis User's Guide*.

Abdelkerim, D. S., Wang, X., Ibrahim, H. A., & Wu, Z. (2019). Static and fatigue behavior of pultruded FRP multi-bolted joints with basalt FRP and hybrid steel-FRP bolts. *Composite Structures*, *220*, 324–337. https://doi.org/10.1016/j.compstruct.2019.03.085

Alagusundaramoorthy, P., Harik, I. E., & Choo, C. C. (2006). Structural Behavior of FRP Composite Bridge Deck Panels. *Journal of Bridge Engineering*, *11*(4), 384–393. https://doi.org/10.1061/(asce)1084-0702(2006)11:4(384)

Ali, H. T., Akrami, R., Fotouhi, S., Bodaghi, M., Saeedifar, M., Yusuf, M., & Fotouhi, M. (2021). Fiber reinforced polymer composites in bridge industry. *Structures*, *30*, 774–785. https://doi.org/10.1016/j.istruc.2020.12.092

Bakis, C., Bank, L. C., & Brown, V. (2002). Fiber-Reinforced Polymer Composites for Construction - State-of-the-Art Review. https://doi.org/10.1061/ASCE1090-026820026:273

Campbell, f. C. (2010). *Structural composite materials*.

Christoforidou, A., Verleg, R., & Pavlovic, M. (2023). Static, fatigue and hygroscopic performance of steel-reinforced resins under various temperatures. *Construction and Building Materials*, *403*, 133079. https://doi.org/10.1016/j.conbuildmat.2023.133079

Composites World. (2020). Pultrusion: The Basics.

Correia, J. R., Branco, F. A., & Ferreira, J. G. (2007). Flexural behaviour of GFRP-concrete hybrid beams with interconnection slip. *Composite Structures*, *77*(1), 66–78. https://doi.org/10.1016/j.compstruct.2005.06.003

Csillag, F. (2018). *Demountable deck-to-girder connection of FRP-steel hybrid bridges* (tech. rep.). http://repository.tudelft.nl/.

Csillag, F., & Pavlović, M. (2021). Push-out behaviour of demountable injected vs. blind-bolted connectors in FRP decks. *Composite Structures*, *270*. https://doi.org/10.1016/j.compstruct.2021.114043

Davalos, J. F., Chen, A., & Zou, B. (2011). Stiffness and Strength Evaluations of a Shear Connection System for FRP Bridge Decks to Steel Girders. *Journal of Composites for Construction*, *15*(3), 441–450. https://doi.org/10.1061/(asce)cc.1943-5614.0000162

ffm-technical-ffm981603-128. (2016). *Fastener + Fixing Magazine*, (98).

InfraCore. (2023). Delamination in FRP.

Joshi, S. C. (n.d.). *The pultrusion process for polymer matrix composites* (tech. rep.).

Jung, D. S., Park, S. H., Kim, T. H., Han, J. W., & Kim, C. Y. (2022a). Demountable Bolted Shear Connector for Easy Deconstruction and Reconstruction of Concrete Slabs in Steel–Concrete Bridges. *Applied Sciences (Switzerland)*, *12*(3). https://doi.org/10.3390/app12031508

Jung, D. S., Park, S. H., Kim, T. H., Han, J. W., & Kim, C. Y. (2022b). Demountable Bolted Shear Connector for Easy Deconstruction and Reconstruction of Concrete Slabs in Steel–Concrete Bridges. *Applied Sciences (Switzerland)*, *12*(3). https://doi.org/10.3390/app12031508

Keller, T., & Gürtler, H. (2005a). Composite Action and Adhesive Bond between Fiber-Reinforced Polymer Bridge Decks and Main Girders. https://doi.org/10.1061/ASCE1090-026820059:4360

Keller, T., & Gürtler, H. (2005b). Quasi-static and fatigue performance of a cellular FRP bridge deck adhesively bonded to steel girders. *Composite Structures*, *70*(4), 484–496. https://doi.org/10.1016/j.compstruct.2004.09.028

Koetsier, M. (2021). *Virtual fatigue verification of Glass Fibre-Reinforced Polymer components for civil engineering applications* (tech. rep.). http://repository.tudelft.nl/.

Krolo, P., Grandić, D., & Bulić, M. (2016). The Guidelines for Modelling the Preloading Bolts in the Structural Connection Using Finite Element Methods. *Journal of Computational Engineering*, *2016*, 1–8. https://doi.org/10.1155/2016/4724312

Kulpa, M., & Siwowski, T. (2019). Stiffness and strength evaluation of a novel FRP sandwich panel for bridge redecking. *Composites Part B: Engineering*, *167*, 207–220. https://doi.org/10.1016/j.compositesb.2018.12.004

Lam, D. (2007). Capacities of headed stud shear connectors in composite steel beams with precast hollowcore slabs. *Journal of Constructional Steel Research*, *63*(9), 1160–1174. https://doi.org/10.1016/j.jcsr.2006.11.012

Mara, V. (2011). *Fibre reinforced polymer bridge decks A feasibility study on upgrading existing concrete-steel bridges* (tech. rep.).

Mara, V., Haghani, R., & Harryson, P. (2014). Bridge decks of fibre reinforced polymer (FRP): A sustainable solution. *Construction and Building Materials*, *50*, 190–199. https://doi.org/10.1016/j.conbuildmat.2013.09.036

Moon Ii, F. L., Ii, ; D. A. E., & Gillespie, J. W. (2002). Shear Stud Connections for the Development of Composite Action between Steel Girders and Fiber-Reinforced Polymer Bridge Decks. https://doi.org/10.1061/ASCE0733-94452002128:6762

Mottram, J. T., & Turvey, G. J. (2003). Physical test data for the appraisal of design procedures for bolted joints in pultruded FRP structural shapes and systems. *Progress in Structural Engineering and Materials*, *5*(4), 195–222. https://doi.org/10.1002/pse.154

NEN. (2021a). *Eurocode 1-Actions on structures-Part 2: Traffic loads on bridges and other civil engineering works* (tech. rep.). www.nen.nl

NEN. (2021b). Eurocode 1-Actions on structures-Part 2: Traffic loads on bridges and other civil engineering works (NB).

Nijgh, M. P. (2017). *New Materials for Injected Bolted Connections A Feasibility Study for Demountable Connections* (tech. rep.).

Nijgh, M. P., & Veljkovic, M. ((2020). Requirements for oversized holes for reusable steel-concrete composite floor systems. *Structures*, *24*, 489–498. https://doi.org/10.1016/j.istruc.2020.01.021

Olivier, G., Csillag, F., Tromp, E., & Pavlović, M. (2021). Conventional vs. reinforced resin injected connectors' behaviour in static, fatigue and creep experiments on slip-resistant steel-FRP joints. *Engineering Structures*, *236*. https://doi.org/10.1016/j.engstruct.2021.112089

Pathirana, S. W., Uy, B., Mirza, O., & Zhu, X. (2016). Bolted and welded connectors for the rehabilitation of composite beams. *Journal of Constructional Steel Research*, *125*, 61–73. https://doi.org/10.1016/j.jcsr.2016.06.003

Pavlović, M. S. (2013). *UNIVERSITY OF BELGRADE FACULTY OF CIVIL ENGINEERING RESISTANCE OF BOLTED SHEAR CONNECTORS IN PREFABRICATED STEEL-CONCRETE COMPOSITE DECKS Doctoral Dissertation* (tech. rep.).

Qureshi, J. (2023). A Review of Fibre Reinforced Polymer Bridges. https://doi.org/10.3390/fib11050040

R. Koloor, S. S., Khosravani, M. R., Hamzah, R. I., & Tamin, M. N. (2018). FE model-based construction and progressive damage processes of FRP composite laminates with different manufacturing processes. *International Journal of Mechanical Sciences*, *141*, 223–235. https://doi.org/10.1016/j.ijmecsci.2018.03.028

Ruben Messelink & Simone Tukker. (2018). Onderhoud van Nederlandse bruggen moet beter, en snel.

Satasivam, S., Feng, P., Bai, Y., & Caprani, C. (2017). Composite actions within steel-FRP composite beam systems with novel blind bolt shear connections. *Engineering Structures*, *138*, 63–73. https://doi.org/10.1016/j.engstruct.2017.01.068

Sotelino, E. D., Teng, M.-H., & Assistant, R. (2001). *Strengthening of Deteriorating Decks of Highway Bridges in Indiana Using FRPC* (tech. rep.).

Szerszen, M. M., & Nowak, A. S. (2000). Fatigue evaluation of steel and concrete bridges. *Transportation Research Record*, *1*(1696), 73–80. https://doi.org/10.3141/1696-10

ter Kuile, J. (2023). *Investigating the behaviour of injected steel-reinforced resin connectors in patch loading tests* (tech. rep.).

Troughton, M. (2008). *Handbook of plastics joining: A practical guide*.

van der Heijden, J. (2023). Vossemeersebrug ruim 2 weken dicht voor werkzaamheden.

van Wingerde, A., van Delft, D., & Knudsen, E. (2002). IBConnectionsvsNormalBolts. *FRC 2002*.

Yang, F., Liu, Y., Jiang, Z., & Xin, H. (2018). Shear performance of a novel demountable steel-concrete bolted connector under static push-out tests. *Engineering Structures*, *160*, 133–146. https://doi.org/10.1016/j.engstruct.2018.01.005

Zhang, Y., Chen, B., Liu, A., Pi, Y. I., Zhang, J., Wang, Y., & Zhong, L. (2019). Experimental study on shear behavior of high strength bolt connection in prefabricated steel-concrete composite beam. *Composites Part B: Engineering*, *159*, 481–489. https://doi.org/10.1016/j.compositesb.2018.10.007

Zhou, A., & Keller, T. (2005). Joining techniques for fiber reinforced polymer composite bridge deck systems. *Composite Structures*, *69*(3), 336–345. https://doi.org/10.1016/j.compstruct.2004.07.016

A

Material Properties Numerical Model

This appendix lists the material properties used for the numerical modelling in this thesis. As the FRP specimens and the reinforced resin are the same as in former projects, this list is based on prior research and MSc projects at the TU Delft (Csillag, 2018; ter Kuile, 2023). Units are in Newton and millimeter, or unitless.

FRP: Lay-up

Web	[-45/45/-45/45/-45/45/0_2/90_2/-45/45/-45/45/-45/45/-45/45]
Sublaminates	[-45/45/-45/45/-45/45/0_2/90_2/45/-45]
Top Facing	[-45/45/-45/45/-45/45/0_2/90_2/45/-45/90_6/0_2/90_2/45/-45/90_6/ 0_2/90_2/45/-45/90_6/0_2/90_2/45/-45/90_6/0_2/90_2/45/-45]

FRP: (Non)linear Elastic Properties

E_1	E_2	E_3	ν_{12}	ν_{13}	ν_{23}	G_{12}	G_{13}	G_{23}
31450	8459	8459	0.272	0.272	0.4	4838	4838	3021

FRP: Hashin Damage Properties

Longitudinal Tensile Stress	Longitudinal Compressive Stress	Transverse Tensile Stress	Transverse Compressive Stress	Longitudinal Shear Stress	Transverse Shear Stress
865	700	36	131	87	75

Longitudinal Tensile Fracture Energy	Longitudinal Compressive Fracture Energy	Transverse Tensile Fracture Energy	Transverse Compressive Fracture Energy
92	80	0.277	0.7979

Steel

Young's Modulus	Poisson's Ratio
210000	0.3

Reinforced Resin with Concrete Plastic Damage Properties

Young's Modulus	Poisson's Ratio	Dilation Angle	Eccentricity	fb0/fc0	K	Viscosity Parameter
16181	0.13	50.535	0.1	1.2	0.78	0

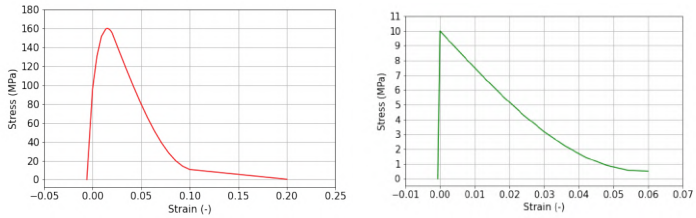

(a) Compression **(b)** Tension

Figure A.1: Material Model SRR (ter Kuile, 2023)

Foam Core

Young's Modulus	Poisson's Ratio	Compression Yield Stress Ratio	Hydrostatic Yield Stress Ratio
2.1	0.2	0.71	0.075

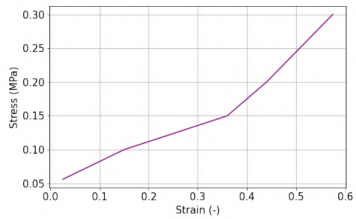

Figure A.2: Foam core in compression (ter Kuile, 2023)

Cohesive Interface - Damage Initiation

Shear Only	Shear-1 Only	Shear-2 Only
21	30	30

Cohesive Interface - Damage Evolution

BK-exponent	Normal Fracture Energy	1st Shear Fracture Enegery	2nd Shear Fracture Energy
2.284	0.9	4	4

B

Design Dimensions

This appendix contains figures regarding the exact dimensions of the spherical coverplate and the FRP deck after production.

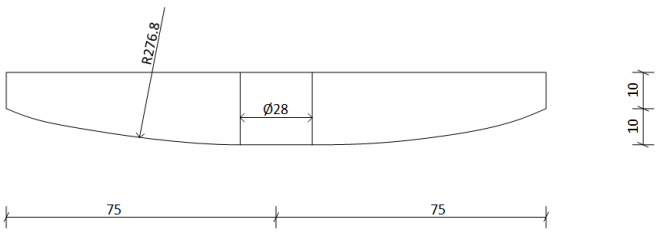

Figure B.1: Dimensions of the spherical plate as used in the experimental campaign

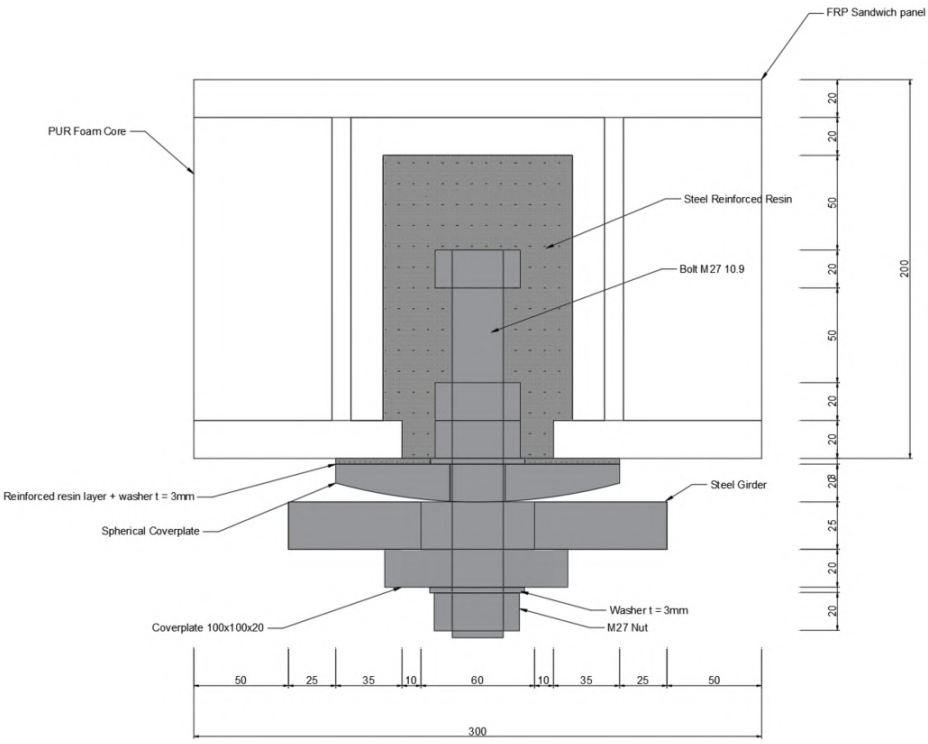

Figure B.2: Cross-section with dimensions of the final design

C

Failure Progression

This appendix displays for tests S1 and S2 three significant moments measured with DIC. The first significant moment of test S2 is denoted as S2.1.

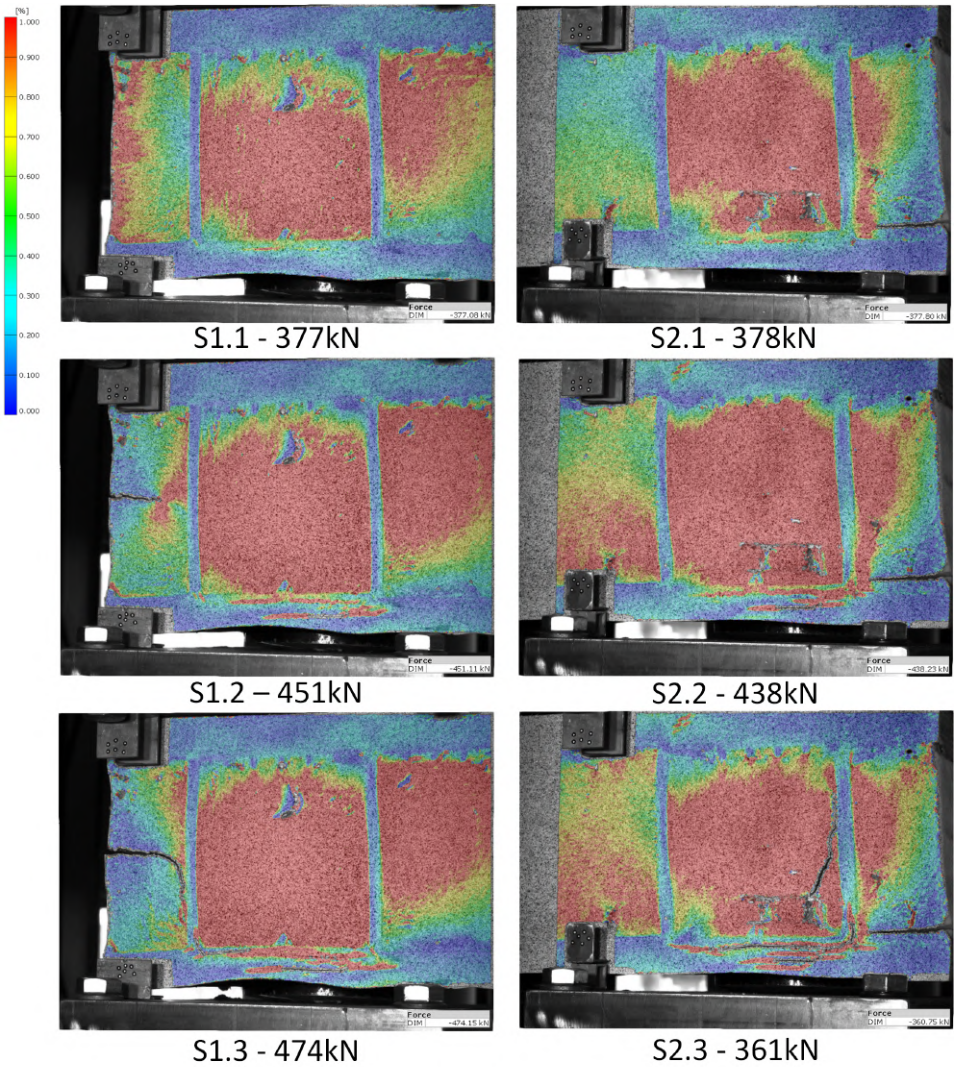

Figure C.1: Failure progression with 1. starting strain in bottom flange, 2. first crack in bottom flange and 3. ultimate failure

D

Cyclic Test Goals

The initial goal for the cyclic tests is to see whether the connector sustains the expected amount of maximum load cycles during a 50 year lifetime. From the analysis in Chapter 3 it follows that the maximum expected load is approximately 85kN following from the 180kN axle in FLM4b. This load model also contains a 170kN axle, extrapolating gives the expected load for this to be 80kN per wheel. Even though it is conservative, it is assumed as that two maximum loads of 85kN are exerted on the connector per truck passing by.
The case-study is located on a roadway, such that the expected amount of trucks in 50 years is (see Table D.1):

$$2\,axles \cdot 0.01 \cdot 500.000\,trucks/year \cdot 50\,years = 500.000 cycles \tag{D.1}$$

Axle Load	% on highway	% on roadway	% on local road	Wheel type
70				A
180				B
170				B
80	1.5	1.0	0.5	C
80				C
80				C
90				C

Table D.1: Heaviest truck from table NB.8 of the Dutch National Appendix to NEN-EN 1991-2+C1 (NEN, 2021b)